Materials Today Bio 32 (2025) 101684

Contents lists available at ScienceDirect

Materials Today Bio

journal homepage: www.journals.elsevier.com/materials-today-bio

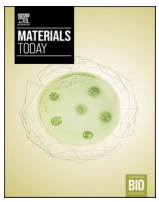

Bufotalin loaded biomimetic nanodrug for combined chemo/photodynamic therapy of cancer

Simin Chen [a,1], Jialong Fan [a,d,1], Qian Xie [e], Yan Qin [a,b], Hailong Xie [c], Chang Xiao [a], Wei Wang [b,*], Bin Liu [a,**]

[a] College of Biology, Hunan University, Changsha, 410082, China
[b] TCM and Ethnomedicine Innovation & Development International Laboratory, School of Pharmacy, Hunan University of Chinese Medicine, Changsha, 410208, China
[c] Hunan Province Key Laboratory of Tumor Cellular & Molecular Pathology, Institute of Cancer Research, School of Medicine, University of South China, Hengyang, 421001, China
[d] Hunan Provincial Key Laboratory of the Research and Development of Novel Pharmaceutical Preparations, Changsha Medical University, Changsha, 410219, China
[e] Hunan Provincial Maternal and Child Health Care Hospital, Hunan Province, Changsha 410008, China

ARTICLE INFO

Keywords:
Cancer
Prussian blue nanoparticles
Bufotalin
Chlorin e6
Combination therapy

ABSTRACT

The combination of chemotherapy and photodynamic therapy (PDT) for enhancing cancer therapeutic efficiency has attracted tremendous attention recently. However, limitations, such as low local concentration and uncontrollable release of therapeutic agents, reduce combined treatment efficacy. In the present study, we engineered a biomimetic nanodrug employing hollow Prussian blue nanoparticles (HPB NPs) to co-load the chemical agent bufotalin (CS-5) and the photosensitizer chlorin e6 (Ce6) for combined chemo/PDT therapy against cancer. HPB NPs with catalase (CAT)-mimetic activity significantly improved the efficacy of PDT by catalyzing the decomposition of H_2O_2 into O_2, thus alleviating hypoxia, which conversely amplified the efficiency of combination therapy. *In vivo* assay demonstrated that the encapsulation of a hybrid membrane on the HPB NPs prolonged blood circulation life 3.4-fold compared to free drug. Additionally, this strategy of combinational chemo/PDT therapy exhibits a remarkable cytotoxic effect against gastric cancer (BGC-823) and breast cancer (4T1) through the induction of ferroptosis and pyroptosis while simultaneously activating the immune response, with minimal adverse effects on normal organs. Thus, the co-delivery system based on biomimetic nanocarriers appears to be a promising platform for combined chemo/PDT therapy in tumor treatment.

1. Introduction

Cancer is among the most formidable diseases individuals encounter today [1]. Conventional cancer treatment modalities, including chemotherapy, surgery, and various other therapeutic approaches, each has inherent limitations that remain unaddressed [2]. For instance, in many cancer cases, tumors and normal tissues are often intertwined, rendering complete surgical removal of tumor cells exceedingly challenging [3]. Conversely, chemotherapy usually results in drug resistance and diminished efficacy due to repeated dosing [4]. Currently, comprehensive therapeutic approaches are employed in clinical settings to achieve satisfactory treatment outcomes by combining multiple modalities.

Bufotalin (CS-5) is a principal active component of the traditional Chinese medicine *Chansu*, a dried secretion from the skin and parotid venom glands of toads [5]. Previous studies have shown that CS-5 exhibits outstanding antitumor activities across in various cancer cells by promoting apoptosis and inhibiting proliferation [6]. In addition, CS-5 triggers apoptosis mediated by p53 in esophageal squamous cell carcinoma cells and induces ferroptosis by promoting the degradation of glutathione peroxidase 4 (GPX4) in A549 non-small cell lung cancer cells [6]. However, its poor water solubility leads to low bioavailability, limiting the clinical application of CS-5. In our previous study, nanomaterials have been adopted to improve its solubility, bioavailability, drug permeability, and regulate the drug release rate by changing the administration pathway to enhance the antitumor activity of CS-5 [7].

* Corresponding author.
** Corresponding author.
E-mail addresses: wangwei402@hotmail.com (W. Wang), binliu2001@hotmail.com (B. Liu).
[1] These authors contributed equally to this work and should be regarded as first authors.

https://doi.org/10.1016/j.mtbio.2025.101684
Received 13 January 2025; Received in revised form 3 March 2025; Accepted 17 March 2025
Available online 18 March 2025

Photodynamic therapy (PDT) represents a non-invasive, spatiotemporally controllable modality that offers the advantages of high selectivity and tumor enrichment, minimal damage to normal tissue, and the potential for repeatable treatment. Consequently, this promising form of therapy has emerged as a research hotspot in the realm of combination therapy for malignant tumors [8]. Nevertheless, the hypoxic tumor microenvironment (TME) significantly undermines the efficacy of PDT. Strategies employing perfluorocarbons (PFCs) for O_2 delivery to the TME have been implemented to enhance PDT treatment outcomes; however, challenges such as limited loading capacity and premature leakage considerably restrict their clinical applicability. Recent investigations have demonstrated that enzyme-mimicking nanomaterials can harness the elevated concentrations of H_2O_2 (50–100 μM) in tumors to catalyze *in situ* O_2 generation via catalase (CAT)-mimetic activity [9,10]. Among them, Prussian blue nanoparticles (PB NPs) have received approval from the FDA for treating radioactive exposure and the sequestration of harmful metal ions from the body. Its good biosafety has been demonstrated in clinical practice [11]. Recently, hollow PB NPs (HPB NPs) have attracted increasing attention due to their remarkable physiological stability, excellent drug-loading capacity, and exceptional CAT-mimetic activity [11]. Thus, HPB NPs present significant potential as nanocarriers for the co-delivery of CS-5 and chlorin e6 (Ce6), providing enhanced therapeutic effects through their dual roles.

Here, we engineered a biomimetic nanodrug employing HPB NPs to co-load the chemical agent CS-5 and photosensitizer Ce6 for combined chemo/PDT therapy against cancer (gastric cancer and breast cancer) (Scheme 1). HPB NPs with CAT-mimetic activity were used as both nanocarrier to load CS-5 and nanocatalyst to induce O_2 generation in hypoxic solid tumors. In the O_2-boosted TME, laser irradiation promoted PDT effect and the CS-5 release efficacy. Furthermore, this strategy could simultaneously induce ferroptosis and pyroptosis in BGC-823 and 4T1 cells. Compared with previous therapeutic approaches based on PDT [12–14], this biomimetic nanodrug presents several advantages: (1) The superior biocompatibility and prolonged circulation half-life of the nanodrug enhance tumor-targeted accumulation, while the CAT-mimetic activity of HPB NPs effectively alleviates tumor hypoxia, thereby amplifying photodynamic generation of singlet oxygen; (2) The oxygen-enhanced PDT synergistically augments CS-5-mediated chemotherapy through ROS production; (3) The concerted induction of ferroptosis and pyroptosis pathways is achieved by these combined

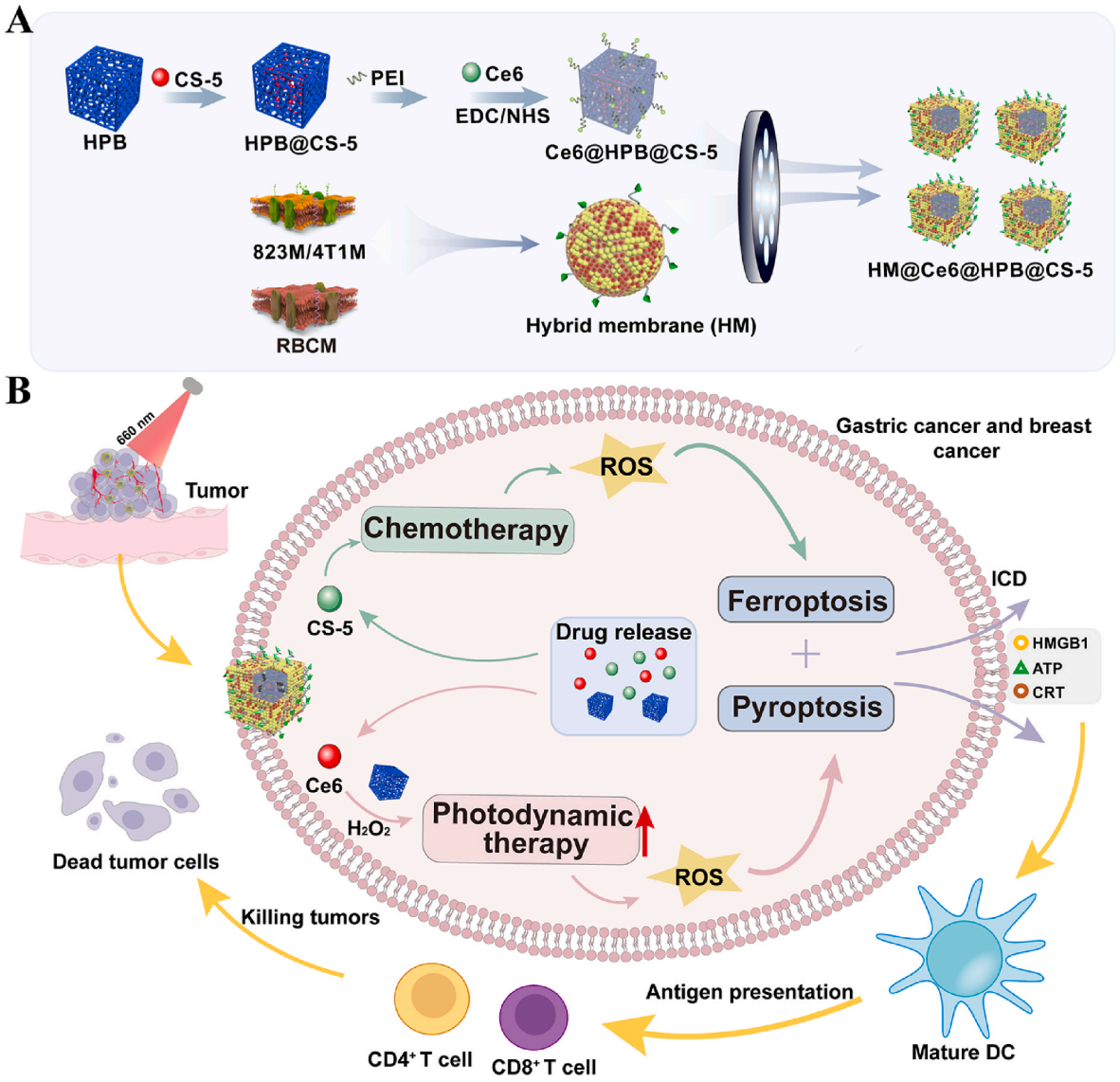

Scheme 1. Schematic illustration for nanodrug synthesis and the underlying mechanism of ferroptosis and pyroptosis-involved cancer cell death via chemo/PDT strategy. (A) Synthetic procedure of HM@Ce6@HPB@CS-5 NPs. (B) Therapeutic mechanisms of HM@Ce6@HPB@CS-5 NPs against cancer through combinational chemo/PDT therapy.

oxidative amplification; (4) This multimodal strategy successfully triggers immunogenic cell death (ICD) while activating antitumor immunity, offering a promising avenue for advancing immunotherapy.

2. Materials and methods

2.1. Materials and reagents

Bufotalin was purchased from Herbest (Xi'an, China). The primary antibodies and secondary antibodies were purchased from Proteintech (IL, USA). K_3 $[Fe(CN)_6]\bullet 3H_2O$ was purchased from Shanghai Aladdin Biochemical Technology Co., Ltd (China). MTT were obtained from Sigma-Aldrich (MO, USA). C11-BODIPY, SOSG, and Chlorin e6 (Ce6) were acquired from Shanghai Maokangbio (Shanghai, China). DCFH-DA, calcein-AM, PI (Propidium Iodide), JC-1 assay kit and BCA protein assay kit were purchased from Yeasen Biotech Co., Ltd (Shanghai, China). Membrane protein extraction kit, DiI (DiIC18(3)), DiO (DiOC18 (3)), ATP assay kit, and LDH assay kit were purchased from Beyotime (Shanghai, China). TMB (3, 3′, 5, 5′-Tetramethylbenzidine), GSH/GSSG assay kit, and MDA assay kit were obtained from Solarbio Science & Technology Co., Ltd (Beijing, China). ELISA assay kits were obtained from NeoBioscience Technology Co., Ltd (Shenzhen, China). The gastric cancer (GC) tissue and paracancerous tissues were obtained from the University of South China.

2.2. Cells and animals

BGC-823, HGC-27, 4T1, SMC, NIH 3T3, HUVEC, and RAW264.7 cells were obtained from Cell Library of Xiangya Central Laboratory. Cells were incubated in a humidified atmosphere at 37 °C with 5 % CO_2. Mice (female, nude BALB/c, 4–5 weeks; female, BABL/c, 4–5 weeks) were purchased from Silaike Experimental Animals Co. Ltd (Hunan). All animal experiments complied with the principles of the "Declaration of Helsinki of the Ministry of Health", and all procedures were executed in accordance with the protocols by the Medical Ethics Committee of Hunan University (SYXK-2023-0010). Clinical GC and paracancerous tissues collection was approved by the University of South China Ethics Committee (NO 2024-114).

2.3. Preparation and characterization of hybrid membrane

Fresh red blood cells (RBCs) from healthy female BALB/c mice were collected with heparin and centrifuged at 4 °C. After washing with PBS, the collected RBCs were placed in cold PBS solution for 2–3 h. The mixture was centrifuged to prepare RBC membrane (RBCM). Finally, the RBCM was harvested according to previous method [15]. Membranes from BGC-823 cells (823M) and 4T1 cells (4T1M) were obtained using a kit for extracting membrane proteins. The hybrid membrane (HM) containing RBCM and 823M (1 mg:1 mg) were obtained under sonication as previously described [16]. The acquisition of 4T1 cell membranes (4T1M) were similar to that of 823M. In subsequent *in vitro* and *in vivo* experiments of breast cancer models, HM represents a hybrid membrane formed by 4T1M and RBCM. In addition, RBCM and BGC-823M solution were stirred with DiI and DiO dyes, respectively, to perform hybrid membrane characterization. The mixture of $RBCM^{DiI}$ and $823M^{DiO}$ were stirred for 30 min. After extruding, the obtained samples were imaged under CLSM (Confocal laser scanning microscopy, Olympus, Japan).

The protein constituents in membranes were determined by SDS-PAGE. After quantifying the protein concentrations of RBCM, BGC-823M, 823M/RBCM (HM), and the membrane of HM@Ce6@HPB@CS-5 NPs, the denatured samples (40 μg/sample) were separated on the 10 % SDS-PAGE. Then, the gel was stained with Coomassie blue for 2 h, washing with distilled water overnight followed by imaging. Meanwhile, the proteins in gel were transferred to PVDF membranes and sequentially incubated with primary antibodies (CD44 and CD47) and secondary antibodies, and then for detected.

2.4. Synthesis and characterization of HPB NPs and HM@Ce6@HPB@CS-5 NPs

PB NPs were synthesized according to the reported method [15]. The prepared PB NPs powder (20 mg) and PVP (100 mg) were mixed in a solution of HCl solution (1 M, 20 mL) and stirred for 2 h. Transfer the mixture to the reaction kettle at 140 °C for 4 h. The collected precipitate was washed repeatedly to obtain HPB NPs. The mixture containing 1 mL HPB (1 mg/mL) and 20 μL CS-5 (5 mg/mL) was stirred overnight and centrifuged to prepare HPB@CS-5 NPs. Next, the mixture containing 1 mg HPB@CS-5 NPs ([HPB] = 1 mg/mL) and 1 mg PEI (4 mg/mL) was stirred for 4 h, followed by centrifuging to obtain the 1 mg HPB@CS-5@PEI NPs ([HPB] = 1 mg/mL). EDC and NHS were adopted to activate the carboxylic group of Ce6 according to the reported method [17,18]. Then, activated-Ce6 (0.02 mg/mL) was added into the HPB@CS-5@PEI NPs ([HPB] = 1 mg/mL) solution to perform a cross-linking reaction for 6 h. After centrifugation, Ce6@HPB@CS-5 NPs were redispersed in PBS. Finally, HM coating on the Ce6@HPB@CS-5 NPs were performed according to the previous method [15] (weight ratio of HM and HPB NPs were 1 mg:1 mg). The morphological characterization, size measurement, and FT-IR spectra assay of NPs were characterized by JEM-2100 microscope (JEOL), dynamic light scattering particle size analyzer (DLS), and Bruker TENSOR27.

HM@Ce6@HPB@CS-5 NPs were stored in PBS or DMEM containing 10 % FBS for 7 days. The sizes of HM@Ce6@HPB@CS-5 NPs were measured at different time points to investigate long-term storage stability.

2.5. The CAT-mimetic and photodynamic properties of M@Ce6@HPB@CS-5 NPs

The CAT-mimetic activity of HM@Ce6@HPB@CS-5 NPs was assessed via the TMB method [19]. In brief, the H_2O_2 was rapidly added to the solution of HM@Ce6@HPB@CS-5 ([HPB] = 15 μg/mL). The absorbance values of the solution at OD_{652nm} were recorded immediately for 4 min. The resulting curves of V_0 against H_2O_2 concentration were fitted using nonlinear regression of the Michaelis–Menten equation. Km and Vmax of CAT-mimetic activity of HM@Ce6@HPB@CS-5 NPs were calculated through the Lineweaver-Burk plot.

0.5 mg HM@Ce6@HPB@CS-5 NPs were mixed with 10 mL H_2O_2 solution (100 mM, pH7.4), and the dissolved O_2 concentration was measured for 4 min with dissolved oxygen meter (JPB-70A). Also, the intracellular O_2 generation capacity of HM@Ce6@HPB@CS-5 NPs was investigated by observing the fluorescence Hypoxia/Oxidative Stress Detection regent as O_2 can strongly quench the fluorescence of this agent [19]. BGC-823 cells in a 96-well plate (1×10^4 cells/well) were cultured under hypoxia (1 % O_2, 5 % CO_2, Anaero-Pack) for 24 h. Then, the cells were incubated with HM@Ce6@HPB@CS-5 NPs ([HPB] = 50 μg/mL, [Ce6] = 1 μg/mL, [CS-5] = 50 nM) for 4 h followed with 660 nm laser irradiation (0.1 W/cm^2) and the addition of H_2O_2 (100 μM). The cells were captured under CLSM.

The $^1O_2$ levels were measured to investigate the capacity of PDT-enhanced $^1O_2$ generation, H_2O_2 (100 μM), the solution of Ce6 or M@Ce6@HPB@CS-5 NPs (100 μL, [Ce6] = 5 μg/mL) were added into the 2, 2, 6, 6-tetramethylpiperidine (TEMP) solution (100 μL, 100 mM). and the mixture was treated with laser (0.1 W/cm^2, 5 min), followed by monitoring with Electron Spin Resonance (ESR) spectrometer (JES-FA 200, Japan).

2.6. Drug loading and controlled release behavior

The same method as described above was used to prepare HPB NPs loaded with CS-5 and PEI@HPB NPs loaded with Ce6. The loaded CS-5 and Ce6 amount were calculated by measuring the absorbance values at

294 nm and 660 nm, respectively. The encapsulation capacity (EC) and loading capacity (LC) were calculated with the following formulas:

$$LC(\%) = \frac{(Mt - Mu)}{Mp} \times 100\%$$

$$EC(\%) = \frac{(Mt - Mu)}{Mt} \times 100\%$$

where Mt indicates the total mass of the drug for loading. Mu represents the mass of not encapsulated drug, and Mp represents the mass of the HPB or HPB@PEI NPs. The NPs (10 mg HPB NPs) were uniformly dispersed into PBS (pH7.4 or pH5.4) and stirred overnight at 37 °C. At predefined time points, the supernatants were collected for UV–vis analysis. After adding an equal amount of PBS (pH7.4 or pH5.4), the mixture was continued to conduct the CS-5 release process. To access the capacity of controlled release of CS-5 under laser irradiation, HM@Ce6@HPB@CS-5 NPs (10 mg) were dispersed in PBS (pH5.4). The solution was treated with 660 nm laser (0.1 W/cm^2) for 5 min, and the release behavior of CS-5 was evaluated according to the above method. The materials dispersed in PBS was performed 4 on/off cycles of laser irradiation.

2.7. Biocompatibility analysis of HPB NPs and HM@Ce6@HPB@CS-5 NPs

NIH 3T3, HUVEC, and SMC were cultured overnight in 96-well plates (5×10^3 cells/well). Then, the medium was substituted with a medium that included HPB NPs or HM@Ce6@HPB@CS-5 NPs. After culturing for another 24 h, the MTT method assessed cell viability. RBCs were mixed with PBS (negative control), deionized water (positive control), HPB, HPB@CS-5, Ce6@HPB@CS-5, and HM@Ce6@HPB@CS-5 NPs (Corresponded to 20, 50, 100 and 200 μg/mL HPB NPs). Following a 4 h incubation at 37 °C, the supernatants at OD_{562nm} was measured. In parallel, RBC morphology was observed under microscope. For platelet aggregation assay, fresh plasma containing platelets was incubated with NPs (100 μg/mL) at 37 °C for 2 h before monitoring the OD_{650nm}.

2.8. Cell uptake, immune escape and penetration of HM@Ce6@HPB@CS-5 NPs

BGC-823 cells in 12-well plates were incubated with HM@Ce6@HPB@CS-5 for 0, 2, 4, 6 or 8 h. After sequentially fixing and staining with DAPI. The cells were performed for CLSM imaging. Meanwhile, quantitative analysis of cell uptake was assessed by flow cytometry (FCM). Then, we determined the immune escape properties of samples by examining the red fluorescence signal after co-incubation of Ce6-loaded materials (Ce6@HPB@CS-5 NPs or HM@Ce6@HPB@CS-5 NPs) with macrophages for 4 h.

The 3D tumor multicellular spheroids (3D MCSs) were cultured by adding each well of SPL Cell Floater Plates (Ultra Low Attachment) with 50 μL of 5×10^3 BGC-823 cells. After 7 days of cultivation, MCSs were incubated with PBS, Ce6, or HM@Ce6@HPB@CS-5 NPs ([HPB] = 50 μg/mL, [CS-5] = 50 nM, [Ce6] = 5 μg/mL) for 6 h. MCSs were imaged under CLSM.

2.9. Cytotoxicity study

Cell viabilities under normoxic and hypoxic conditions were investigated, respectively. Briefly, BGC-823 cells (8×10^3 cells/well) were treated with different materials in normoxic or hypoxic conditions. The cells were cultured for another 4 h followed by laser irradiation (660 nm, 0.1 W/cm^2, 3 min). MTT assay was performed 20 h later to assess the cell viability. For live/dead stain assay, BGC-823 cells were treated with different NPs and irradiated, whereas others were not. After a further 20 h, calcein-AM (10 μg/mL) and PI (5 μg/mL) were added for 30 min, and the cells were imaged under CLSM. MCSs were incubated with PBS, Ce6, CS-5 and HM@Ce6@HPB@CS-5 NPs ([HPB NPs] = 50 μg/mL, [Ce6] = 1 μg/mL, [CS-5] = 50 nM) for twice. MCSs were imaged by an inverted microscope over 8-days. Following a 1 h incubation with calcein-AM (10 μg/mL) and PI (5 μg/mL), the MCSs were washed with PBS and transferred to confocol dishes for imaging with CLSM.

2.10. Intracellular ROS and LPO accumulation assay

The BGC-823 cells in 6-well plates incubated overnight were treated with HM@Ce6@HPB@CS-5 NPs ([HPB NPs] = 50 μg/mL, [CS-5] = 50 nM, [Ce6] = 1 μg/mL) for 6 h. DCFH-DA (10 μM) was added and incubated for 30 min, followed by laser irradiation (660 nm, 0.1 W/cm^2, 3 min). Intracellular ROS levels were imaged under CLSM.

BODIPY581/591-C11 (Invitrogen, USA) was used as the probe to detect the LPO accumulation in cells [20]. Briefly, BGC-823 cells were treated using the above method. Then, the cells were stained with BODIPY-C11 according to the protocol for imaging with CLSM.

2.11. Measurement of mitochondrial membrane potential

BGC-823 cells treated for 4 h with HM@Ce6@HPB@CS-5 NPs and irradiated with laser irradiation (660 nm, 0.1 W/cm^2, 3 min). The cells were stained with JC-1 according to the protocol for imaging with CLSM.

2.12. Intracellular GSH and MDA assay

BGC-823 cells were treated with PBS, Ce6, CS-5, HM@Ce6@HPB@CS-5 ([HPB NPs] = 50 μg/mL, [CS-5] = 50 nM, [Ce6] = 1 μg/mL) and treated with 660 nm laser (0.1 W/cm^2, 3 min). After culturing for 24 h, the cells were collected, and the GSH and MDA level in the supernatants were evaluated using GSH/GSSG assay kit and MDA assay kit according to the instruction's manual.

2.13. Cell membrane integrity assay

BGC-823 cells were incubated with PBS, Ce6, CS-5, HM@Ce6@HPB@CS-5 ([HPB NPs] = 50 μg/mL, [CS-5] = 50 nM, [Ce6] = 1 μg/mL) with or without 660 nm laser (0.1 W/cm^2, 3 min). After incubating for 6 h, the cells were stained with T11 and DAPI; the cells were observed by CLSM.

2.14. Detection of intracellular hypoxia level

The hypoxia levels in cells were detected using a hypoxia/oxidative stress detection kit (Enzo Life Sciences), according to previous methods [14]. Briefly, BGC-823 cells were treated with different formulations ([HPB NPs] = 50 μg/mL, [CS-5] = 50 nM, [Ce6] = 1 μg/mL, [H_2O_2] = 100 μM) and then put in an Anaero-Pack (1 % O_2) for 4 h with or without laser irradiation (660 nm, 0.1 W/cm^2, 3 min). The cells were washed with PBS; the detection mix was added according to the procedure; the cells were captured by CLSM.

2.15. Western blot assay

BGC-823 or 4T1 cells were incubated with PBS, Ce6, CS-5 and HM@Ce6@HPB@CS-5 NPs ([HPB NPs] = 50 μg/mL, [CS-5] = 50 nM, [Ce6] = 1 μg/mL) before 660 nm laser irradiation (0.1 W/cm^2, 3 min). The cells were lysed in the cold RIPA buffer. The concentration of supernatants was quantified by BCA assay. Samples were separated on the 10 % SDS-PAGE gel, and the proteins were transferred to PVDF membranes and sequentially incubated with primary antibodies (GAPDH, GPX4, Caspase-3, GSDME) and secondary antibodies. The levels of proteins were detected using an ECL chromogenic solution. The gastric cancer tissues and corresponding paraneoplastic tissues from the

University of South China were lysed with RIPA, and the level of GPX4 was detected following the methodology mentioned above.

2.16. In vivo biodistribution images and pharmacokinetics

BGC-823-bearing nude mice were intravenously injected with different NPs ([HPB] = 5 mg/kg, [Ce6] = 2.5 mg/kg, [CS-5] = 0.5 mg/kg). The fluorescence image was captured at predetermined time points to observe the biodistribution profiles of Ce6@HPB@CS-5 and HM@Ce6@HPB@CS-5 NPs. Major organs were isolated from the euthanized mice for imaging at 48 h post-injection.

After administration with Ce6, Ce6@HPB@CS-5 NPs, and HM@Ce6@HPB@CS-5 NPs ([HPB NPs] = 5 mg/kg, [Ce6] = 2.5 mg/kg; [CS-5] = 0.5 mg/kg) into healthy BABL/c mice, the blood was taken from the mice at different times. Then, the serum obtained from whole blood was further imaged by the Kodak multimode imaging system to conduct a pharmacokinetics assay.

2.17. The bone marrow-derived dendritic cells (BMDCs) maturation in vitro

To study the maturation of BMDCs, BMDCs were isolated from the bone marrow of female BABL/c mice (4–6 weeks old) and cultivated in a medium containing GM-CSF and IL-4 for 7 days *in vitro*. The BGC-823 cells were treated for 24 h to acquire specific media, followed by an additional 24 h incubation with BMDCs. The BMDCs were labeled with anti-PE-CD80 and anti-FITC-CD86 antibodies and examined using FCM. The cell supernatant samples were collected to identify cytokines (TNF-α, IL-6) using ELISA kits.

2.18. Anti-tumor efficacy and immunity study in vivo

The BGC-823 cells (1×10^7 cells per mouse) were subcutaneously injected into the back of female nude BALB/c mice to construct gastric cancer models. The BGC-823 model mice with tumor volume of 100 mm^3 were randomly divided into 4 groups (n = 5), including PBS, Ce6+L, CS-5, HM@Ce6@HPB@CS-5+L ([HPB NPs] = 5 mg/kg, [Ce6] = 2.5 mg/kg, [CS-5] = 0.5 mg/kg). The mice were intravenously injected with different samples every two days. Local laser irradiation (L) (660 nm, 0.1 W/cm^2, 5 min) was applied 12 h after injection. The body weight and tumor size were monitored every two days. After administration, the mice were sacrificed for collecting tumors and other organs.

Meanwhile, 4T1 cells were orthotopically implanted into the fourth abdominal mammary fat pads of BABL/c mice. And the breast cancer model mice with tumor volume of 100 mm^3 were randomly divided into 3 groups (n = 5), including PBS, CS-5, HM@Ce6@HPB@CS-5+L ([HPB NPs] = 5 mg/kg, [Ce6] = 2.5 mg/kg, [CS-5] = 1 mg/kg). The mice were intravenously injected with different samples every two days. Local laser irradiation (L) (660 nm, 0.1 W/cm^2, 5 min) was applied 12 h after injection. The body weight and tumor size were monitored every two days. After administration, the mice were sacrificed, and excised tumor tissues were weighed and imaged. The tumors were analyzed by metastasis markers (MMP-9), hypoxia markers (HIF-1α), and ferroptosis biomarker (GPX4) analysis. The blood samples were collected for routine biochemistry analysis.

Tumors were excised from mice and embedded in paraffin for immunofluorescence staining. Subsequently, partial tumors without fixed were processed into single cell suspensions. Finally, single-cell suspensions were stained with anti-CD16/32, zombie aqua, APC/Cyanine7-CD45, APC-CD11b, FITC-CD3, Percp/Cy-5.5-CD4, BV785-CD8a, PE-Foxp3, and PE/Cy7-CD25 antibodies (Biolegend) and analyzed by FCM.

2.19. Transcriptomics analysis

For assessing the mRNA levels in BGC-823 cells, transcriptomics analysis was performed after treatment with PBS, CS-5 (50 nM), and HM@Ce6@HPB@CS-5 NPs with laser ([HPB NPs] = 50 μg/mL, [CS-5] = 50 nM, [Ce6] = 1 μg/mL) for 24 h. Total RNA extraction was performed with the TRIZOL, followed by sequencing of transcriptome libraries using Oebiotech. Differential expression was assessed using DESeq. A fold change of 2:1 or greater and a false discovery rate-corrected *P* value of 0.05 or less were used as thresholds for differential genes.

2.20. Statistical analysis

Statistical analyses were performed using GraphPad Prism 9.0.0 software (USA). Differences between groups were estimated by the one-way ANOVA, representing at least three independent experiments. The statistical significance was set at $^*P < 0.05$, $^{**}P < 0.01$, and $^{***}P < 0.001$.

3. Results and discussion

3.1. CS-5 can inhibit GPX4 expression in GC cells

Bufotalin (CS-5) is a steroid lactone that contains four carbon skeleton rings and one lactone ring [21], the structure of which is shown in Fig. 1A. MTT assay demonstrated the strong cell-killing effect on gastric cancer (GC) cell lines including BGC-823 and HGC-27 cells with IC_{50} value of 45.9 nM and 130.4 nM, respectively (Fig. 1B). Bufotalin has been reported to efficiently kill tumor cells by inhibiting the expression of GPX4 [22]. The pronounced elevation of GPX4, a pivotal marker of ferroptosis within tumor tissue, is intricately linked to an unfavorable prognosis in cancer patients [23].Thus, we further investigated the clinical significance of GPX4 expression in GC using the GEPIA 2 website. The results showed a significant increase of GPX4 in GC tissues compared to normal tissues (Fig. 1C). Furthermore, GC patients with high GPX4 expression generally exhibited significantly lower overall survival rates compared to those with low GPX4 levels (Fig. 1D). By performing Western blot analysis on clinical tissue samples, it was also found that seven GC tissues exhibited higher GPX4 levels than the paracancerous tissues (Fig. 1E). Afterward, utilizing the BGC-823 cell line as a model, we observed a CS-5 concentration-dependent inhibition on GPX4 expression (Fig. 1F). By combining with RNA-seq assay and analyzing the data using gene set enrichment analysis (GSEA), a noteworthy enrichment of differentially expressed genes in the ferroptosis and a significant decrease in GPX4 mRNA level was found in BGC-823 cells with CS-5 treatment (Fig. 1G and H). These results indicate that CS-5 can efficiently kill GC cells via inducing ferroptosis.

3.2. Synthesis and characterization of HM@Ce6@HPB@CS-5 NPs

To enhance the efficacy of CS-5 while reducing the potential cardiotoxicity, we constructed a biomimetic nanoparticle loaded with CS-5 and Ce6 to perform combinational chemo/PDT against tumor. The detailed synthesis process for HM@HPB@CS-5@Ce6 NPs is illustrated in Scheme 1. A variety of characterization methods were utilized to elucidate the properties of HM@Ce6@HPB@CS-5 NPs. Transmission electron microscopy (TEM) images showed the cubic-like HPB NPs with an approximate diameter of 100 nm (Fig. 2A). The HM@Ce6@HPB@CS-5 NPs clearly revealed similar core-shell nanostructure, with a diameter of approximately 110 nm, showcasing a membrane layer thickness about 5.5 nm (Fig. 2B). Consistent with TEM images, DLS assay indicated the average sizes of 106 nm for HPB NPs and 120 nm for HM@Ce6@HPB@CS-5 NPs due to the membrane coating (Fig. 2C). This result demonstrated that camouflaged of hybrid membrane can slightly affect the size of NPs [24]. The UV–vis spectra revealed distinct peaks at 710 nm, 294 nm, and 410 nm, characteristic of HPB NPs, CS-5, and the hybrid membrane, respectively (Fig. 2D). Notably, new peaks at 660 nm and 400 nm appeared in the HM@Ce6@HPB@CS-5 NPs, indicative of the modification by Ce6 [12] and hybrid membrane [24] (Fig. 2D). Zeta

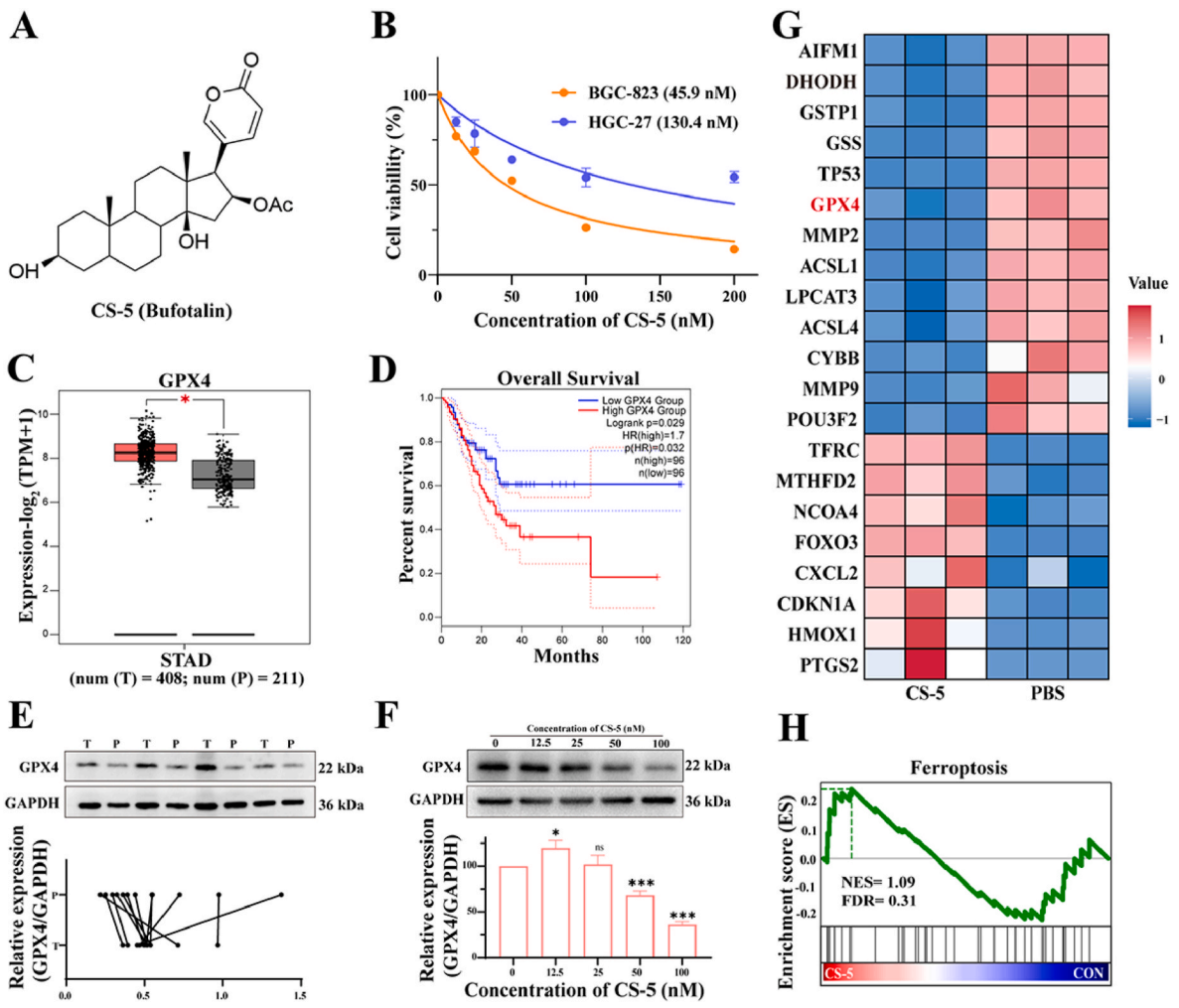

Fig. 1. CS-5 induces ferroptosis in GC cells *in vitro*. (A) The pharmaceutical structure of CS-5. (B) The cell viabilities of BGC-823 and HGC-27 cells with CS-5 treatment. (C) Relative expression and quantitative analysis of GPX4 in GC tissues (T) and paracancerous tissues (P) from GEPIA 2. (D) Disease free survival assay of GC patients with different GPX4 levels based on GEPIA 2. (E) Western blot and quantitative analysis of GPX4 in GC tissue (T) and paracancerous tissues (P) ($n = 12$). (F) Relative expression of GPX4 in BGC-823 cells treatment with CS-5. (G) Heatmap representing the levels of various genes in BGC-823 cells (Blue: low expression; Red: high expression). (H) GSEA for ferroptosis signaling pathway in BGC-823 cells after treatment with CS-5 ($n = 3$). $^{*}P < 0.05$, $^{***}P < 0.001$. *ns*, not significant.

potentials of HPB NPs and Ce6@HPB@CS-5 NPs were measured to be −4.5 mV and 0.5 mV, respectively. Following camouflaging with the hybrid membrane, the zeta potential changed from positive to negative (−6.2 mV) (Fig. 2E). FT-IR spectra demonstrated the characteristic peak of $Fe^{2+}C{\equiv}N\text{-}Fe^{3+}$ at 2086 cm^{-1} in HPB NPs [16], while Ce6@HPB@CS-5 NPs showed new characteristic peaks at 1561 cm^{-1} and 1718 cm^{-1}, corresponding to the amide (CO=N-) stretching vibrations after cross-linking with Ce6 [12,25] (Fig. S1A). This provided compelling evidence for the successful conjugation of Ce6 to the PEI of HPB NPs. In addition, utilizing the fluorescence imaging, we observed intense yellow fluorescence in the HM group resulting from the merging of red fluorescence emitted by $RBCM^{DiI}$ and green fluorescence emitted by $823M^{DiO}$ (Fig. 2F), thus confirming the successful fusion of RBCM and 823M cells.

Considering the tumor-targeting capability and low immunogenicity of 823M, along with the prolonged blood circulation half-life conferred by RBCM, the optimal ratio of 823M:RBCM was determined to be 1:1 for subsequent experiments [24]. Fig. 2G demonstrated the inherited protein profiles of the hybrid membrane in HM@Ce6@HPB@CS-5 NPs originating from RBCM and 823M, consistent with the previous reports [16]. Western blotting analysis further confirmed the existentence of CD44 and CD47 in 823M/RBCM of HM@Ce6@HPB@CS-5 NPs, the corresponding protein markers for 823M and RBCM, respectively (Fig. S1B), which was similar to HM. Stability assay demonstrated a homogeneous dispersion and good stability of HM@Ce6@HPB@CS-5 NPs for at least 7 days, without significant change in size when suspended in PBS or DMEM supplemented with 10 % FBS (Fig. 2H). This stability is crucial for minimizing drug leakage during systemic circulation [26].

We subsequently investigated the ratio effect of drug/HPB NPs on the entrapment efficiency. According to the feeding ratio of 0.1:1 and 1:1, the entrapment efficiencies of CS-5 and Ce6 in HPB NPs were determined to be 2.9 % and 99 %, respectively (loading efficiency were 0.3 % and 95.8 %, respectively) (Figs. S1C and S1D). Next, by monitoring the release behavior, we found that the release of CS-5 showed pH- and laser-dependent manners. The release rate of CS-5 was only about 16.2 % over 48 h under pH7.4 condition, which was lower than that of pH5.5 (28.3 %) (Fig. S1E). However, the released CS-5 reached 54 % at pH5.5 condition after 4 rounds of 660 nm laser irradiation (0.1 W/cm^2, 5 min) (Fig. S1F). Therefore, under simulated TME conditions and following laser irradiation, morphological characterization of HM@Ce6@HPB@CS-5 NPs was performed. TEM analysis revealed distinct structural disruption of the membrane (Fig. S1G). These findings aligning with prior reports [19,24], indicated a controlled release manner of CS-5 from HM@Ce6@HPB@CS-5 NPs attributable to the

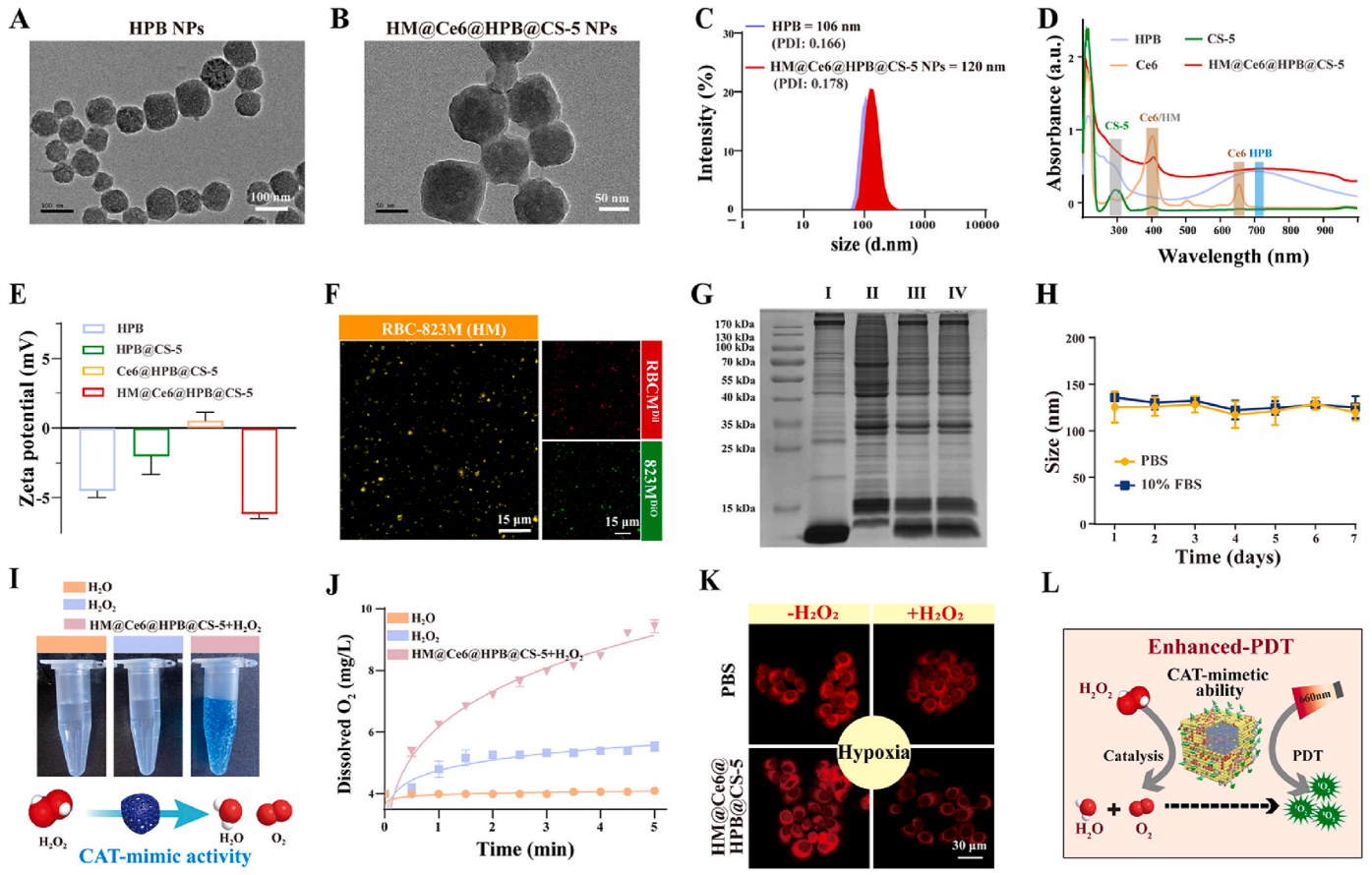

Fig. 2. Preparation and physicochemical properties of HM@Ce6@HPB@CS-5 NPs. TEM images of HPB NPs (A) and HM@Ce6@HPB@CS-5 NPs (B). (C) Size distribution of HPB NPs and HM@Ce6@HPB@CS-5 NPs measured by DLS. (D) UV–vis spectra of HPB NPs, Ce6, CS-5, HM@Ce6@HPB@CS-5. (E) The zeta potentials of HPB, HPB@CS-5, Ce6@HPB@CS-5, HM@Ce6@HPB@CS-5. (F) CLSM images of hybrid membrane. (G) SDS-PAGE analysis of RBCM, BGC-823M, HM and membrane of HM@Ce6@HPB@CS-5 NPs. I: RBCM; II: BGC-823M; III: HM; IV: membrane of HM@Ce6@HPB@CS-5 NPs. (H) The size of HM@Ce6@HPB@CS-5 in PBS and DMEM containing 10 % FBS at different time. (I and J) The images and dissolved O_2 concentration change of different components. (K) Fluorescence images of BGC-823 cells treated with PBS, H_2O_2, HM@Ce6@HPB@CS-5, HM@Ce6@HPB@CS-5+H_2O_2 in hypoxia. (L) Scheme of $^1O_2$ (ROS) generation caused by PDT. Data are expressed as mean ± SD ($n = 3$).

structure of HPB NPs and disruption of the hybrid membrane. This release manner can not only fulfill the requirement of high drug concentration in the tumor region but also reduce side effects on normal tissues [27]. Taken together, the above results affirmed the successful synthesis of HM@Ce6@HPB@CS-5 NPs, which are essential for realizing a combinational chemo/PDT for tumor eradication.

We have reported the intrinsic CAT-like activity of HPB NPs [28]. In this study, we investigated whether the different modification can affect the CAT-mimetic activity of HPB NPs using TMB method. TMB can be oxidized by H_2O_2 to form ox-TMB with a maximum absorption peak at 652 nm in the presence of catalase [29]. Consistent with our previous findings [28], UV spectra analysis indicated an increase of OD_{652nm} in the presence of HM@Ce6@HPB@CS-5 NPs. Meanwhile, the absorbance values at OD_{652nm} showed a positive relation with H_2O_2 concentration within 0.5–5 mM (Fig. S1H). Through enzymatic kinetics studies, the Km and Vmax values of HM@Ce6@HPB@CS-5 NPs were calculated to be 0.634 mM and 3.32×10^{-4} Ms^{-1}, respectively (Figs. S1I and S1J). Notably, the Km value for HM@Ce6@HPB@CS-5 NPs was lower than those of reported AuNCs-NH_2 (10.6 mM) [30] and Co_3O_4 nanorods (4.82 mM) [31], suggesting it possesses high catalytic efficiency. Subsequently, we explored the O_2 generation capacity of HM@Ce6@HPB@CS-5 NPs. Fig. 2I and J visually indicated the rapid appearance of bubbles (O_2) in the HM@Ce6@HPB@CS-5 NPs + H_2O_2 group and the gradual increase of O_2 content with the time extension in anaerobic water. We then investigated the impact of HM@Ce6@HPB@CS-5 NPs with O_2 generation function on the hypoxic state within tumor cells. At first, anaerobic cultivation was adopted to create a hypoxia environment for BGC-823 cells according to the previous method [28]. Then, the hypoxia probe, which can emit red fluorescence [19], was applied to illustrate the intracellular hypoxia levels of tumor cells. As we expected, BGC-823 cells treated solely with HM@Ce6@HPB@CS-5 NPs exhibited a strong red fluorescence signal, indicative of cellular hypoxia. In contrast, only a weak red signal was observed in the BGC-823 cells following the addition of H_2O_2 in conjunction with HM@Ce6@HPB@CS-5 NPs (Fig. 2K). These results compellingly demonstrated that HM@Ce6@HPB@CS-5 NPs effectively mitigate cellular hypoxia by catalytically decomposing H_2O_2 into O_2 (Fig. 2L). This property is particularly advantageous for PDT, as it alleviates the hypoxic conditions that often impede therapeutic efficacy within tumors. To further identify the type of ROS generated during PDT, ESR spectra were used to detected the $^1O_2$ signal (distinct 1:1:1 triplet signal). In the HM@Ce6@HPB@CS-5 NPs + H_2O_2+L group, the highest $^1O_2$ signal can be detected, whereas a weaker peak was observed in the Ce6+L and HM@Ce6@HPB@CS-5 NPs + L group (Fig. S1K). In contrast, H_2O_2+L group displayed negligible $^1O_2$ signal. This result revealed that the introduction of H_2O_2 for HM@Ce6@HPB@CS-5 NPs were effective in producing $^1O_2$.The $^1O_2$ generation mechanism underlying oxygen enhanced-PDT is delineated in Fig. 2L.

3.3. Anti-tumor effect of HM@Ce6@HPB@CS-5 NPs

Fluorescence imaging revealed time-dependent cellular uptake of

HM@Ce6@HPB@CS-5 NPs in BGC-823 cells, with red fluorescence intensity gradually increasing and reaching a plateau at 4 h (Fig. 3A). FCM assay further confirmed these findings (Fig. 3B), suggesting efficient cellular entry consistent with our previous work [15]. Considering that NPs with immune escape can prolong the *in vivo* circulation time of drugs, we then explored the effect of macrophages on the uptake behavior of HM@Ce6@HPB@CS-5 NPs. Figs. S2A and S2B showed that the red fluorescence signal in HM@Ce6@HPB@CS-5 NPs-treated macrophages was 2.16-fold higher than that of Ce6@HPB@CS-5 NPs-treated macrophages at the concentration of 50 μg/mL. This phenomenon demonstrated the ability of membranes-coated NPs to evade the surveillance and clearance of immune cells [32]. Then, we investigated the homing targeting effect of HM@Ce6@HPB@CS-5 NPs on various tumor cells. As expected, 4T1 cells showed weak fluorescence signals following incubation with all NPs. In contrast, both 823M@Ce6@HPB@CS-5 NPs and HM@Ce6@HPB@CS-5 NPs-treated cells showed strong red fluorescence in BGC-823 cells, which is higher than that of the RBCM@Ce6@HPB@CS-5 NPs-treated group (Fig. 3C). These findings suggest that the tumor cell membrane endowed good targeting capability of HM@Ce6@HPB@CS-5 NPs to BGC-823 cells. Consistent with previous report [24], the hybrid membrane comprised of 4T1 and RBCM only exhibited excellent targeting effect on 4T1 tumor cells. In addition, by examining the penetration ability of HM@Ce6@HPB@CS-5 NPs using MCSs *in vitro*, we found that HM@Ce6@HPB@CS-5 NPs exhibited more intense red fluorescence signals in the central part of the MCSs of BGC-823 cells, in comparison to the Ce6@HPB@CS-5 NPs-treated group (Figs. S2C and S2D). We hypothesize that this phenomenon could be attributed to the homologous targeting capability of HM@Ce6@HPB@CS-5 NPs and an antigenic library derived from 823M cells, which facilitates their deep penetration into MCSs [33]. These results demonstrate that hybrid membrane encapsulation considerably boosts the penetration efficiency of Ce6@HPB@CS-5 NPs.

Next, we investigated the cancer cell killing ability of HM@Ce6@HPB@CS-5 NPs plus laser irradiation under hypoxia, the condition significantly compromised the effectiveness of PDT [28]. Consistent with this report, MTT assay indicated that the viability of

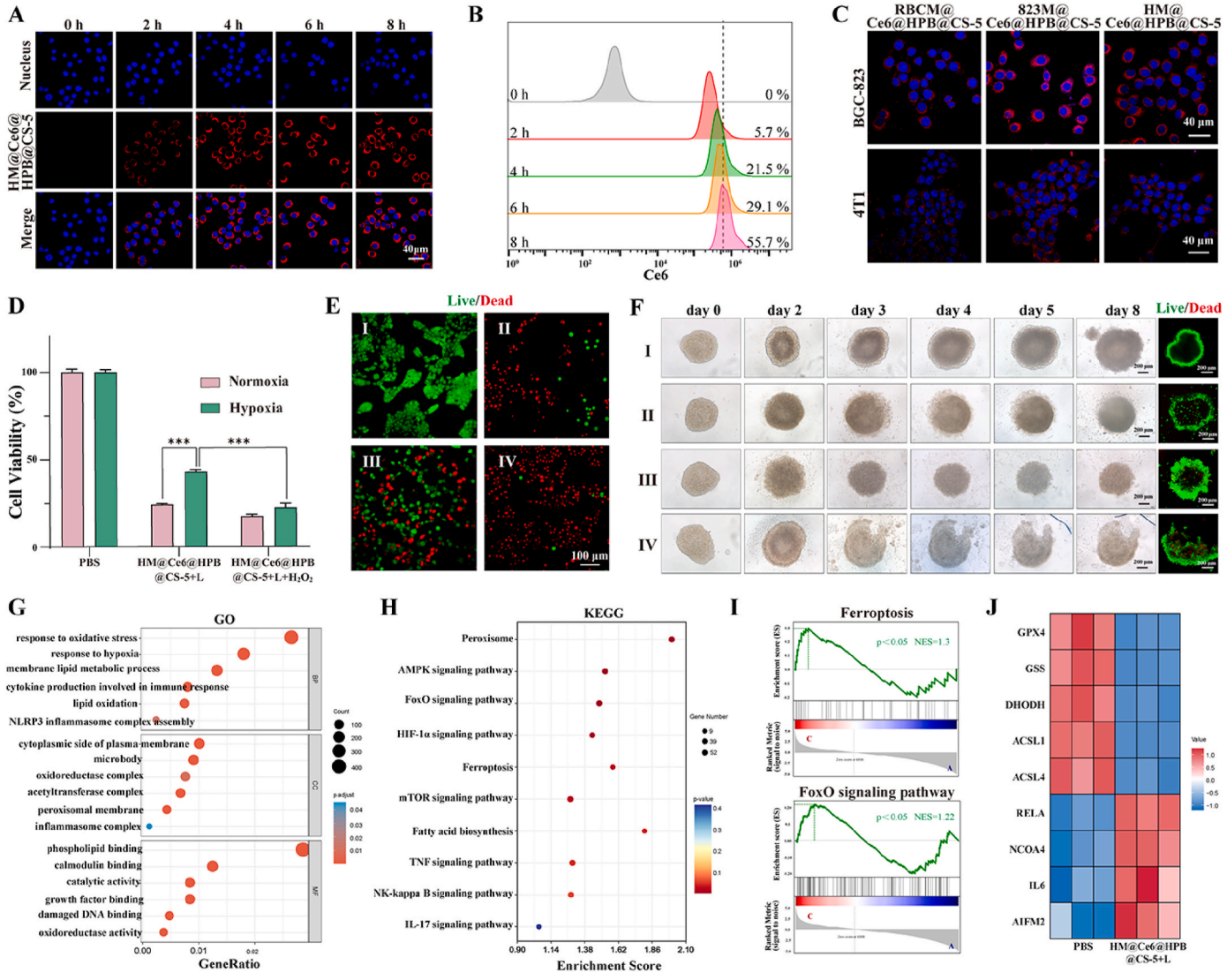

Fig. 3. HM@Ce6@HPB@CS-5 NPs can induce ferroptosis and pyroptosis in BGC-823 cells. (A) Fluorescence images of BGC-823 cells co-cultured with different NPs over time, respectively. (B) FCM analysis and relative quantitative analysis of cell uptake efficacy of HM@Ce6@HPB@CS-5 NPs in BGC-823 at different time points. (C) CLSM images of BGC-823 cells and 4T1 cells upon incubation with HM@Ce6@HPB@CS-5, 823M@Ce6@HPB@CS-5 and RBCM@Ce6 @HPB@CS-5 for 6 h. (D) The effect of O_2 concentration on the BGC-823 cell viability. (E) Live/dead imaging of BGC-823 cells after with different treatments (660 nm, 0.1 W/cm^2, 3 min). I: PBS, II: Ce6+L, III: CS-5, IV: HM@Ce6@HPB@CS-5+L. (F) Representative images and live/dead imaging of 3D MCSs with different treatments. I: PBS, II: Ce6+L, III: CS-5, IV: HM@Ce6@HPB@CS-5+L. (G) GO analysis. (H) KEGG analysis. (I) GSEA for ferroptosis and FoxO signal pathways. (J) Heatmap representing the levels of ferroptosis and pyroptosis genes in BGC-823 cells ($n = 3$). Data are expressed as mean ± SD, $n = 3$. ***$P < 0.001$.

BGC-823 cells administered with Ce6+L (1 μg/mL) under hypoxia was significantly higher than that of normoxia (85.7 % *vs.* 40.0 %) (Fig. S2E). However, in the presence of 100 μM of substrate H_2O_2, the viability of BGC-823 cells administered HM@Ce6@HPB@CS-5+L was comparable to that of cells under normoxia (22.3 % *vs.* 24.3 %) (Fig. 3D and S2F). This result suggested that the hypoxia alleviation caused by HPB NPs enhanced the cytotoxicity of PDT, which is highly advantageous for achieving an effective tumor-killing effect. Calcein-AM/PI staining analysis also showed that HM@Ce6@HPB@CS-5+L treatment resulted in approximately 80 % cell mortality (Fig. 3E). In addition, fluorescence imaging based on 3D MCSs, an accurate model for simulating tumor internal environment, indicated the improvement of hybrid membrane coating on the penetrating ability of HPB NPs (Fig. S2D). Moreover, after 8 days of treatment, the HM@Ce6@HPB@CS-5+L group exhibited the highest accumulation of cellular debris, the most pronounced disruption within the tumor bulb, and significant limitation of tumor growth (Fig. 3F). In contrast, the MCSs in the Ce6+L and CS-5 treatment groups exhibited minimal loosening. Moreover, the volume of MCSs was maintained with a slight tendency to change. The live/dead staining of 3D MCSs further confirmed the enhanced tumor-killing efficacy of the HM@Ce6@HPB@CS-5+L treatment (Fig. 3F). These findings indicate that HM@Ce6@HPB@CS-5+L treatment effectively disrupts the structure of MCSs and induces internal tumor cell death.

3.4. RNA sequencing analysis

RNA sequencing assay was adopted to investigate the gene expression change in BGC-823 cells caused by HM@Ce6@HPB@CS-5 NPs + L, so as to explore the underlying mechanisms of the antitumor effect. The principal component analysis (PCA) plot indicated good repeatability of samples for assay (Fig. S3A). The Venn diagram revealed that 12923 genes were co-expressed in these two groups, with 344 genes being exclusively expressed in the M@Ce6@HPB@CS-5 NPs + L-treated group (Fig. S3B). According to the criterion of *p*-value being <0.05, we identified a total of 11484 differentially expressed mRNAs, comprising 5655 upregulated and 5829 downregulated genes between HM@Ce6@HPB@CS-5 NPs + L and PBS group (Fig. S3C). Gene ontology (GO) analysis indicated that deferentially expressed genes were highly enriched in the process of oxidative stress, lipid oxidation, and inflammasome complex (Fig. 3G), KEGG analysis further demonstrated the significant enrichment of genes related with ferroptosis, NF-κB, AMPK, and IL-17 signaling pathways (Fig. 3H). And the GSEA

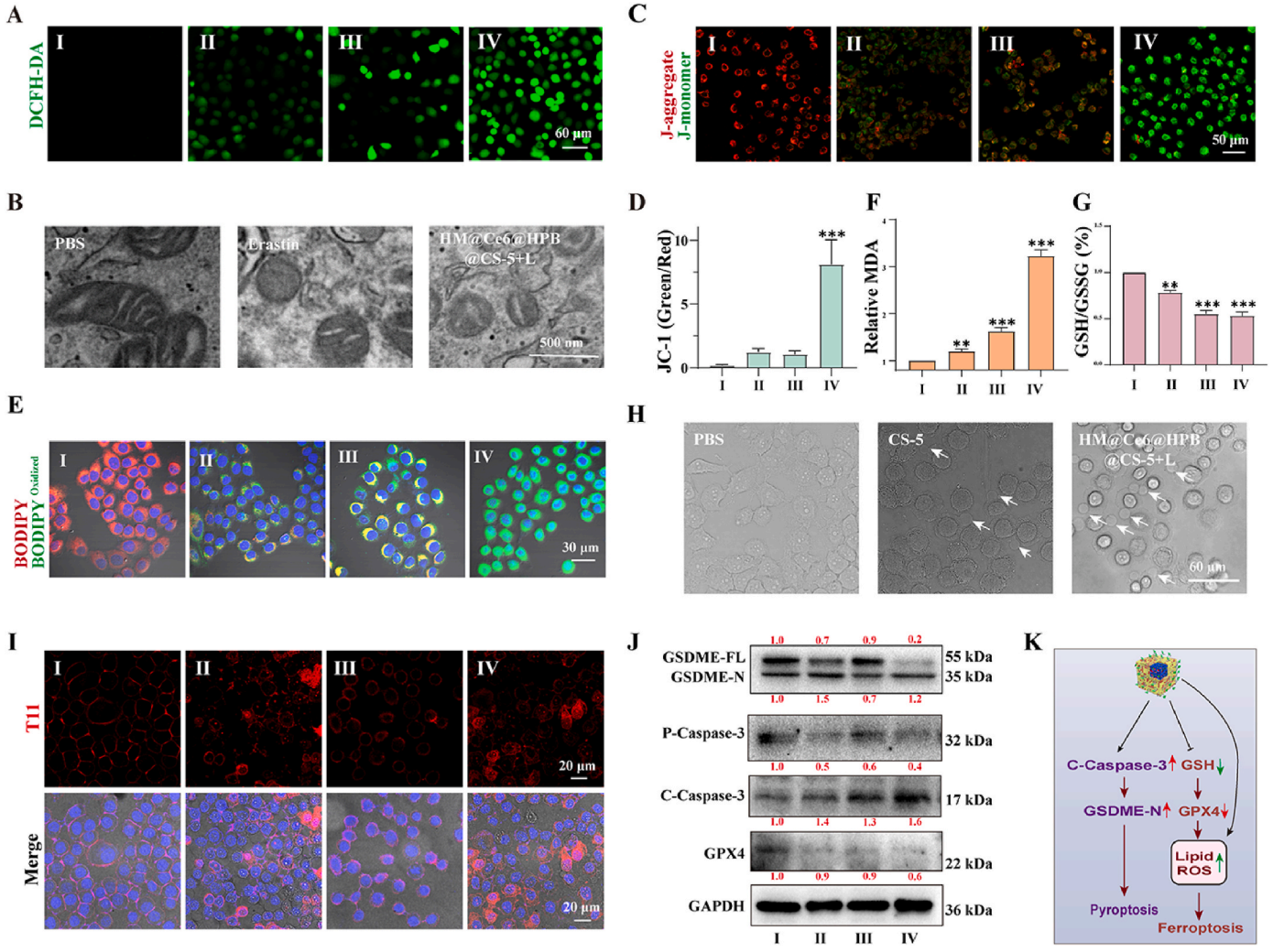

Fig. 4. HM@Ce6@HPB@CS-5 NPs can induce ferroptosis and pyroptosis in BGC-823 cells. (A) ROS images of BGC-823 cells after with different treatments. (B) Bio-TEM image of the BGC-823 cell treatment with PBS, erastin, HM@Ce6@HPB@CS-5+L. (C and D) The CLSM images and the quantitative result of mitochondrial membrane potential in the BGC-823 cell treated with Ce6+L, CS-5 and HM@Ce6@HPB@CS-5+L. (E) LPO level of BGC-823 cells. (F) Relative MDA level in BGC-823 cells. (G) The GSH/GSSG assay of BGC-823 cells. (H) The images of BGC-823 cell morphology change after various treatments. (I) Observation of ruptured cell membrane by CLSM. (J) Western blot of GSDME, Caspase-3 and GPX4 in BGC-823 cells. (K) Schematic illustration of HM@Ce6@HPB@CS-5+L induced ferroptosis and pyroptosis. I: PBS, II: Ce6+L, III: CS-5, IV: HM@Ce6@HPB@CS-5+L. Data are expressed as mean ± SD ($n = 3$), $^{*}P < 0.05$, $^{**}P < 0.01$, $^{***}P < 0.001$.

analysis revealed a notable enrichment of differentially expressed genes related to ferroptosis and FoxO signal pathway (related to pyroptosis and oxidative stress [34]) (Fig. 3I), suggesting the important roles of ferroptosis and pyroptosis caused by HM@Ce6@HPB@CS-5 NPs + L in killing tumor cells. Moreover, key genes of ferroptosis and pyroptosis including NCOA4, AIFM2, DHODH, GPX4, GSS, ACSL2, ACSL4, RELA and IL-6 showed significant change in BGC-823 cells with HM@Ce6@HPB@CS-5 NPs + L treatment (Fig. 3J).

3.5. HM@Ce6@HPB@CS-5 NPs trigger ferroptosis and pyroptosis by mitochondrion damage

Mitochondrion damage caused by ROS is closely related to ferroptosis and pyroptosis [35,36]. We first examined the changes in ROS levels in BGC-823 cells treatment with HM@Ce6@HPB@CS-5 NPs. As shown in Fig. 4A, the most intense green fluorescence was shown in HM@Ce6@HPB@CS-5+L group. This phenomenon was mechanistically attributed to PDT effect of Ce6 combined with CS-5-induced oxidative stress. Meanwhile, the morphological change of mitochondria from long strips to points and the less or disappearance of cristae was found in the cells with HM@Ce6@HPB@CS-5+L treatment, which was consistent with the erastin group, a ferroptosis inducer (Fig. 4B). High ROS can result in the disappearance of membrane potential by damaging the mitochondrial structure. Fluorescence imaging based on JC-1 probe showed significant green fluorescence in tumor cells with HM@Ce6@HPB@CS-5+L treatment due to the mitochondrial structure damage. In contrast, PBS treated cells emitted red fluorescence of JC-1 aggregates (Fig. 4C and D). These results demonstrate that the mitochondria have suffered significant damage after treated with HM@Ce6@HPB@CS-5 NPs + L. Next, using C11 BODIPY as the lipid peroxidation (LPO) sensor, we explore the levels of LPO, a well-established biomarker of ferroptosis. This sensor can exhibit a shift in fluorescence emission peak from red to green upon oxidation [37]. As shown in Fig. 4E, the membranes of BGC-823 cells with HM@Ce6@HPB@CS-5+L treatment showed the strongest green fluorescence and weakest red fluorescence signal compared with the CS-5 group and the Ce6 group due to the richest accumulation of LPO. The significant increase of malondialdehyde (MDA), an LPO marker, in this group further confirmed LPO accumulation (Fig. 4F). GSH, crucial cofactor of the GPX4 to detoxify LPO and safeguard cells against ferroptosis [38], was downregulated by CS-5 (Fig. 4G). Meanwhile, PDT-mediated enhancement of ROS and the following disruption of the dynamic cellular redox balance significantly reduced the GSH/GSSG ratio in BGC-823 cells.

According to previous studies, the increase in ROS induced by PDT may trigger acute inflammation and cause pyroptosis [39]. Interestingly, from the cellular morphology, we observed the appearance of pyroptosis in BGC-823 cells, as shown in Fig. 4H. The cells exhibited swelling accompanied by protrusions (bubbles), characteristic features of cell pyroptosis. The pore-forming mechanism of pyroptosis includes the cell membrane integrity disruption, release of contents including pro-inflammatory molecules and antigens [36]. The T11 dye selectively stains proteins in the cytoplasm in HM@Ce6@HPB@CS-5 NPs-treated cells, indicating that the HM@Ce6@HPB@CS-5 NPs can effectively destroy the integrity of the cell membrane through the combination effect of CS-5 and PDT (Fig. 4I). In addition, it was found that the levels of cell contents and cytokines, such as lactate dehydrogenase (LDH) and IL-1β released from HM@Ce6@HPB@CS-5+L treated cells were strongly higher than those of CS-5 treated cells (Figs. S4A and S4B). Western blot assay further demonstrated the downregulation of ferroptosis marker of GPX4 and the upregulation of pyroptosis marker of GSDME-N in the BGC-823 cells subjected to the same treatment. Consistent with the previous report [40], the occurrence of pyroptosis directly upregulated the levels of cleaved-caspase-3 (Fig. 4J). These findings suggested that the combination strategy could efficiently kill tumor cells by inducing ferroptosis and pyroptosis (Fig. 4K).

3.6. HM@Ce6@HPB@CS-5 stimulated the maturation of BMDCs in vitro

The anti-tumor immunity activation can be elicited by damage-associated molecular pattern signals (DAMPs) released from dying cancer cells undergoing immunogenic cell death [41] (Fig. 5A). Benefiting from the prominence of HM@Ce6@HPB@CS-5 NPs-mediated ferroptosis and pyroptosis in BGC-823 cells, we further investigated their effect on the induction of ICD. Notably, both CS-5 and HM@Ce6@HPB@CS-5+L significantly induced the exposure of CRT on the surface of tumor cells. The green fluorescence intensity of CRT in BGC-823 cells treated with HM@Ce6@HPB@CS-5+L was 10.8-fold and 1.7-fold higher than that in cells treated with PBS and CS-5, respectively (Fig. 5B and D). Meanwhile, the decrease of red fluorescence intensity within nucleus reflected the release of HMGB1 (Fig. 5C and D). Additionally, HM@Ce6@HPB@CS-5+L treatment significantly increased ATP secretion of tumor cells (Fig. 5E). Consequently, we examined the alterations in morphology and maturation-related indicators of DCs. The images of mature BMDCs in HM@Ce6@HPB@CS-5+L group exhibited an increase in cell surface protrusions with pronounced branching (Fig. 5F). The co-culture of supernatants from pre-treated BGC-823 cells treated with HM@Ce6@HPB@CS-5+L increased the number of mature BMDCs (28.8 %) (Fig. 5F and G). Meanwhile, ELISA assay revealed that the levels of IL-6 and TNF-α from mature BMDCs increased by 2.5-fold and 3.8-fold in the CS-5 group, and 3.0-fold and 4.6-fold in the HM@Ce6@HPB@CS-5+L group, respectively, compared to PBS group (Fig. 5H and I). This revealed a significant increase in BMDCs in the HM@Ce6@HPB@CS-5+L group. These findings demonstrated that HM@Ce6@HPB@CS-5+L significantly facilitated the maturation of BMDCs, thereby potentially augmenting anti-tumor immune responses to combat GC.

3.7. Combinational therapy significantly inhibited gastric tumor growth

The targeting capability is crucial for enhancing the effectiveness of therapeutic agents in tumor treatment. Following intravenous (*i.v.*) administration, BGC-823-bearing mice were subjected to imaging at 0.5, 4, 6, 9, 12, 24, and 48 h. *In vivo* fluorescence images indicated that the signal in the tumor region of the mice gradually increased following the administration of HM@Ce6@HPB@CS-5 NPs within 12 h post-injection and the signal sustained at least 48 h due to the accumulation of NPs. In contrast, the signal in the mice administered with Ce6@HPB@CS-5 NPs began to decline at 12 h post-administration (Fig. 6A and S5A). Both fluorescence imaging and quantitative assay of tumor tissue showed stronger fluorescence in the HM@Ce6@HPB@CS-5 NPs group compared to the Ce6@HPB@CS-5 NPs group (Fig. 6B and S5B). These results reflected the homologous targeting capability of HM@Ce6@HPB@CS-5 NPs [42,43]. Meanwhile, a strong fluorescence signal was observed in the kidney of mice administered Ce6@HPB@CS-5 NPs, which may aid in mitigating the toxicity of HM@Ce6@HPB@CS-5 NPs during long-term usage. Consistent with this result, the half-life of HM@Ce6@HPB@CS-5 NPs was prolonged 2.6-fold and 3.4-fold, compared to the Ce6@HPB@CS-5 NPs and Ce6, respectively (Fig. 6C and S5C). These results reveal that membrane coating significantly prolongs blood circulation time with enhancing targeting ability *in vivo*.

Next, we examined the anti-tumor efficiency of HM@Ce6@HPB@CS-5 on BGC-823 tumor-bearing mice. The tumor-bearing mice were divided randomly into five groups: PBS (control group), Ce6+L, CS-5, and HM@Ce6@HPB@CS-5+L. As indicated in Fig. 6D, the NPs were injected intravenously, and the laser irradiation group was exposed to 660 nm laser irradiation (0.1 W/cm^2) for 5 min at 12 h post-injection. During the experiment, the mice behaved normally without significant weight change (Fig. 6E), indicating that our dosage was within the normal range. The tumor growth curve revealed rapid growth of tumors in the PBS group, whereas mice subjected to therapeutic interventions exhibited differential tumor growth inhibition.

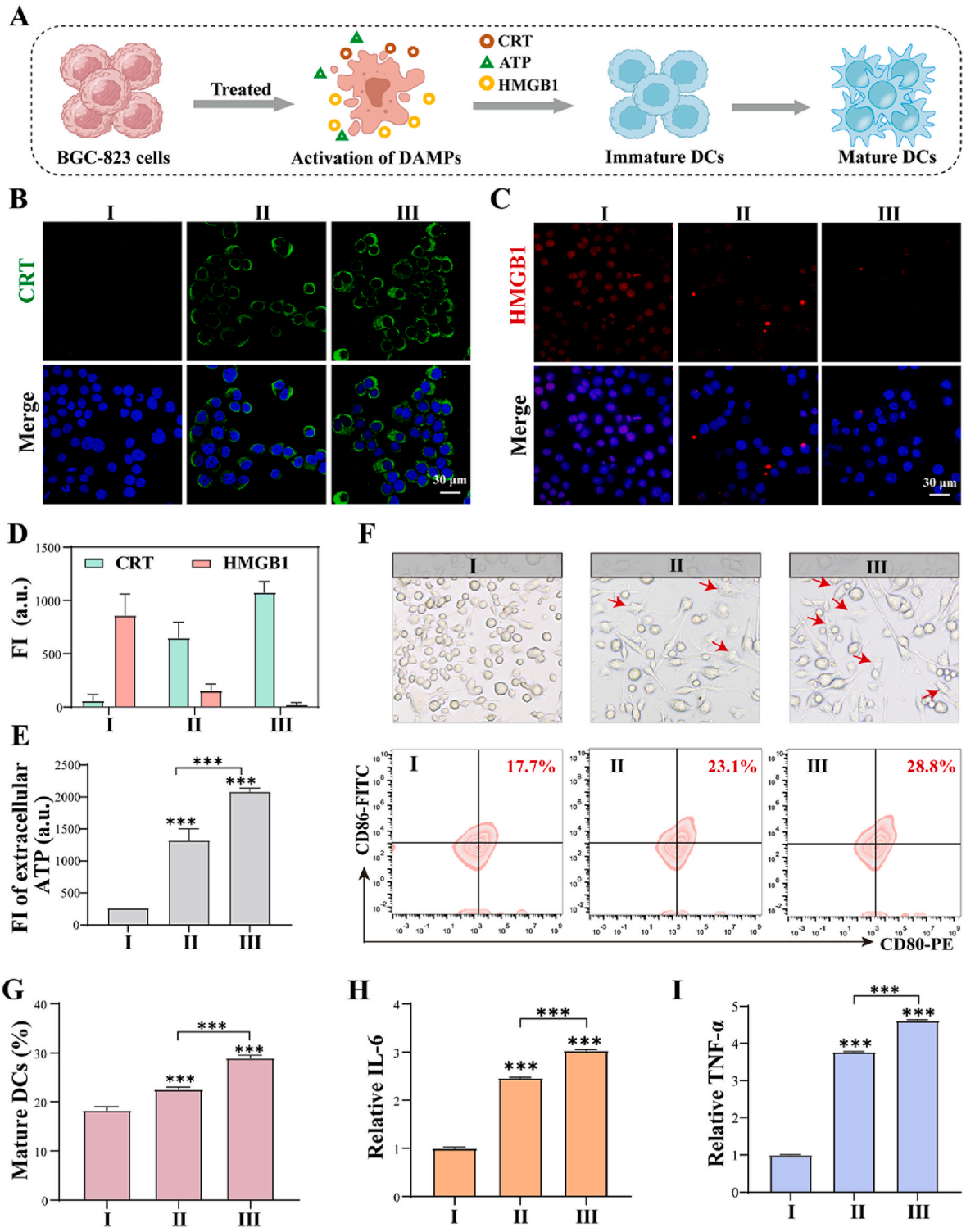

Fig. 5. HM@Ce6@HPB@CS-5 NPs induces ICD. (A) Experimental procedure to induce the maturation of BMDCs. (B–D) The levels of CRT and HMGB1 of BGC-823 cells after PBS, CS-5 and HM@Ce6@HPB@CS-5 treatment. (E) The ATP level of BGC-823 cells after different treatments. (F and G) Microscopy images, representative FCM plots and proportions of mature BMDCs ($CD11c^+$ $CD80^+$ $CD86^+$) after different treatments. (H and I) ELISA assay for IL-6 and TNF-α proinflammatory cytokines. I: PBS, II: CS-5, III: HM@Ce6@HPB@CS-5+L. Data are expressed as mean ± SD ($n = 3$), $^{***}P < 0.001$.

Notably, mice treated with HM@Ce6@HPB@CS-5+L demonstrated the slowest tumor growth (Fig. 6F), attributable to the combinational effects of PDT and CS-5. Fig. 6G visually indicated the most potent anti-tumor effect in the HM@Ce6@HPB@CS-5+L group. The quantitative assay demonstrated a tumor growth inhibitory rate of more than 86.0 % in this group (Fig. 6H), which is higher than that of CS-5 (21 %) and Ce6+L (33.6 %), which was attributed to the HM@Ce6@HPB@CS-5 NPs integrating CS5 and Ce6 together and their targeting capability. H&E staining showed massive area of cell necrosis (dotted area) after HM@Ce6@HPB@CS-5+L treatment (Fig. 6I). Immunostaining indicated the most significant decrease of GPX4 in the HM@Ce6@HPB@CS-5+L group, compared to other groups, demonstrating the highest

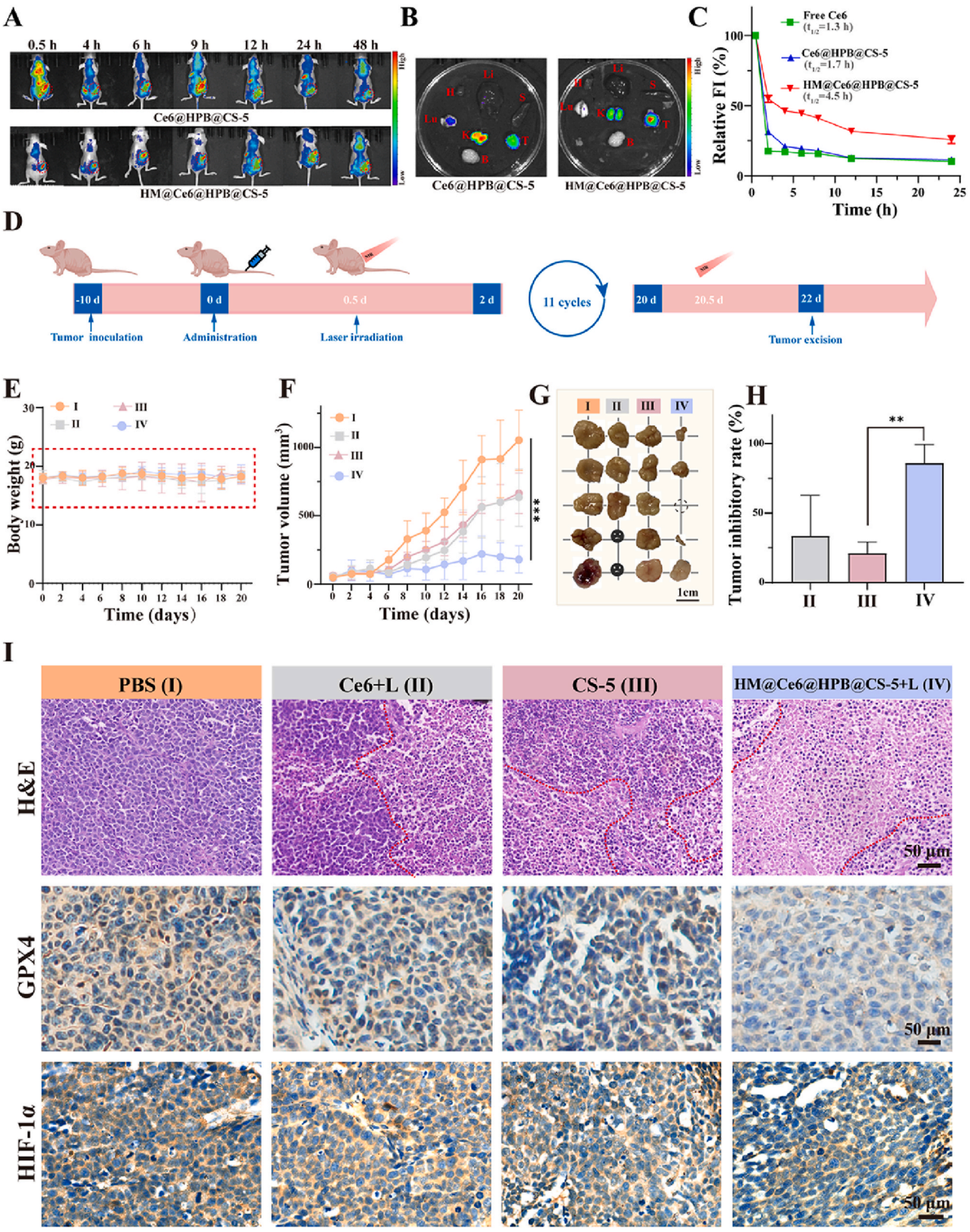

Fig. 6. *In vivo* combinational chem/PDT therapy against BGC-823 tumors. (A) The biodistribution of Ce6-loaded NPs in BGC-823 tumor-bearing nude BALB/c mice at different time points. (B) *Ex vivo* fluorescence images of excised tumor and major organs at 48 h post-administration. (C) The quantification of half-life. (D) Schematic diagram of treatment *in vivo*. (E) Body weight change curve of BALB/c during treatment period ($n = 5$). (F) The tumor growth curve with various treatments. (G) The digital images of tumors. (H) The tumor inhibition rate of mice. (I) Histological analysis of tumor section stained with H&E, GPX4 and HIF-1α ($n = 3$). I: PBS, II: Ce6+L, III: CS-5, IV: HM@Ce6@HPB@CS-5+L. Data are expressed as mean ± SD ($n = 3$–5). $^{*}P < 0.05$. $^{**}P < 0.01$. $^{***}P < 0.001$.

ferroptosis levels in tumor tissue (Fig. 6I). Additionally, the *in vivo* study demonstrated the alleviation of tumor hypoxia, which was reflected by the low expression of HIF-1α (Fig. 6I). In contrast, no significant change was found for this protein in the mice treated with sole PDT. This result demonstrated that HM@Ce6@HPB@CS-5+L could improve the therapy efficacy by attenuating hypoxia and promoting ferroptosis.

3.8. Anti-tumor effect and immune responses induced by combinational therapy on breast cancer

To widen the application of this strategy for tumor therapy, we investigated the effect of HM@Ce6@HPB@CS-5 NPs+L on breast cancer. Drawing upon the *in vitro* experimental findings that illustrate the immunostimulatory property of HM@Ce6@HPB@CS-5 NPs, 4T1 cells were chosen for subsequent *in vivo* anti-tumor and immunological experiments. Before initiating *in vivo* treatment, the ability of HM@Ce6@HPB@CS-5 NPs to induce both ferroptosis and pyroptosis in 4T1 cells was confirmed by Western blot analysis, exhibiting GSDME-N upregulation and GPX4 downregulation (Fig. S6A). Similarly, HM@Ce6@HPB@CS-5 NPs+L treatment successfully induced CRT exposure and HMGB1 translocation from the nucleus to the cytoplasm (Figs. S6B–E).

Further, the 4T1-bearing mice were subsequently treated via tail vein administration of PBS, CS-5, and HM@Ce6@HPB@CS-5 NPs when the tumor volume reached 100 mm^3 (Fig. 7A). In comparison to the PBS group, the CS-5 administration partially inhibited tumor growth due to the rapid elimination and passive tumor accumulation *in vivo*. In contrast, HM@Ce6@HPB@CS-5 NPs+L exhibited the highest tumor inhibitory effect (Fig. 7B). This result demonstrated that the combinational strategy had a significant *in vivo* therapeutic effect on the breast cancer (Fig. 7B–D). Fig. S7A indicated stable body weight of all mice throughout the treatment process. H&E staining results indicated the damaged morphology of the tumor cells in the HM@Ce6@HPB@CS-5+L group, which reflected the strongest killing ability for *in situ* tumors (Fig. 7E). Additionally, the GPX4, HIF-1α, and MMP-9 levels were significantly reduced (Fig. S7B), aligning with results observed in the subcutaneous model of GC. The IL-6 and IL-1β levels in the HM@Ce6@HPB@CS-5+L group were significantly higher than other groups (Figs. S7C and S7D). Moreover, a distant tumor model was established to evaluate the inhibitory effect of HM@Ce6@HPB@CS-5. Fig. 7F indicated that the number of distant tumors in HM@Ce6@HPB@CS-5 NPs + L group was lower than that of PBS group (3 *vs.* 5) (Fig. 7G–H). H&E staining exhibited the strongest killing ability of HM@Ce6@HPB@CS-5+L in the distant tumor tissue (Fig. 7I), aligning with *in situ* tumor. It is noteworthy that 4T1-bearing mice are highly susceptible to lung metastasis due to the highly malignant nature of breast cancer cells [44]. However, HM@Ce6@HPB@CS-5 NPs + L administration significantly inhibited lung metastasis of breast cancer (Fig. 7J). H&E staining demonstrated few metastatic lesions in lung tissues of mice with HM@Ce6@HPB@CS-5 NPs + L treatment (Fig. 7J). Compared to the PBS group, the inhibitory rate reached 92 %, according to the quantitative assay of metastatic nodules in the lung. Meanwhile, sole CS-5 was found to slightly inhibit breast cancer lung metastasis (Fig. 7K). Overall, HM@Ce6@HPB@CS-5 NPs + L administration significantly inhibited the growth of both primary and distant tumors and effectively suppressed lung metastasis. Accordingly, we detected the capability of HM@Ce6@HPB@CS-5 NPs in inducing ICD in the breast cancer model. Fig. 7L indicated that the HM@Ce6@HPB@CS-5 NPs group showed the strongest CRT signal and lowest HMGB1 signal compared to other treatment groups, the result of which reflected the induction of high-level ICD. FCM analysis further indicated that the percentages of $CD4^+$ T cells in the tumor tissues of HM@Ce6@HPB@CS-5+L group (58.8 %) were significantly higher than those of other groups (PBS group: 18.6 %, CS-5 group: 50.8 %) (Fig. 7M and P). And the HM@Ce6@HPB@CS-5+L treatment increased the proportion of $CD8^+$ T cells ($CD3^+$ $CD8^+$) (29.0 %) compared to the PBS group (4.8 %) and CS5 group (11.5 %) (Fig. 7N and P). Meanwhile, the proportions of immunosuppressive regulatory T cells (Tregs, $CD25^+$ $Foxp3^+$) in the tumor tissue of mice treated with HM@Ce6@HPB@CS-5+L, CS-5 and PBS were 9.43 %, 17.9 % and 33.6 %, respectively (Fig. 7O and P). These results demonstrated that HM@Ce6@HPB@CS-5+L could induce ICD, enhance immune cell penetration, and decrease Tregs infiltration *in vivo*, thereby inhibiting the growth of both primary and distant tumors.

3.9. The toxicity evaluation

Finally, we evaluated the toxicity of NPs *in vitro* and *in vivo*. MTT assay demonstrated 80 % viability for three normal cell lines (NIH 3T3 cell, SMC cell, and HUVEC cell) with HM@Ce6@HPB@CS-5 NPs even at the concentration of 100 μg/mL (Figs. S8A and S8B). In addition, the blood compatibility of HM@Ce6@HPB@CS-5 NPs, which is crucial for clinical application, was evaluated. Clear supernatants in the RBC solution and negligible hemolysis (hemolysis rate <8 %) of HM@Ce6@HPB@CS-5 NPs treatment at a high concentration of 200 μg/mL were shown in Fig. S8C and Fig. S8D. Meanwhile, intact morphology of RBC and negligible platelet aggregation were found after co-incubation with HM@Ce6@HPB@CS-5 NPs (Figs. S8E and S8F), confirming the high hemocompatibility of HM@Ce6@HPB@CS-5. H&E staining showed no pathological alterations or abnormalities in the organs of mice with HM@Ce6@HPB@CS-5 administration (Fig. 8A). In addition, no significant difference was found for the indicators of WBC, RBC, PLT, HGB, MCV and PDW of mice with HM@Ce6@HPB@CS-5+L administration, compared with normal level (Fig. 8B–G). The liver and kidney function indicators in the HM@Ce6@HPB@CS-5+L group were comparable to those of the PBS group (Fig. 8H and I), further revealing that our strategy has toxic effects on mice. Above results suggested the elevated biocompatibility and biosafety of HM@Ce6@HPB@CS-5 NPs *in vivo*.

4. Conclusion

In summary, by preparing HM@Ce6@HPB@CS-5 NPs, we have developed a highly efficient chemo/PDT therapy strategy for cancer therapy. The HM@Ce6@HPB@CS-5 NPs enhanced the targeting ability and half-life of the drug through the biomimetic membrane coating, thereby increasing drug concentration at the tumor site. Moreover, the CAT-like activity of HPB NPs alleviates tumor hypoxia, enhancing the therapeutic effect of PDT. Additionally, the combination of PDT with CS-5 amplified ROS production and induced pyroptosis and ferroptosis, thereby leading to ICD to promote the maturation of DCs and subsequent activation of T cells for anti-tumor effects. The multifunctionality of HM@Ce6@HPB@CS-5 NPs holds promise in addressing the tumor penetration and hypoxia in PDT-related clinical applications, overcoming the limitations of single therapy, and providing a promising treatment strategy for clinical cancer therapy.

CRediT authorship contribution statement

Simin Chen: Writing – original draft, Investigation, Data curation, Conceptualization. **Jialong Fan:** Writing – original draft, Validation, Methodology, Funding acquisition, Data curation, Conceptualization. **Qian Xie:** Methodology, Investigation, Funding acquisition. **Yan Qin:** Supervision, Methodology, Funding acquisition. **Hailong Xie:** Supervision, Resources, Methodology. **Chang Xiao:** Validation, Methodology, Data curation. **Wei Wang:** Supervision, Project administration. **Bin Liu:** Writing – review & editing, Supervision, Project administration, Funding acquisition, Conceptualization.

Declaration of competing interest

The authors declare that they have no known competing financial

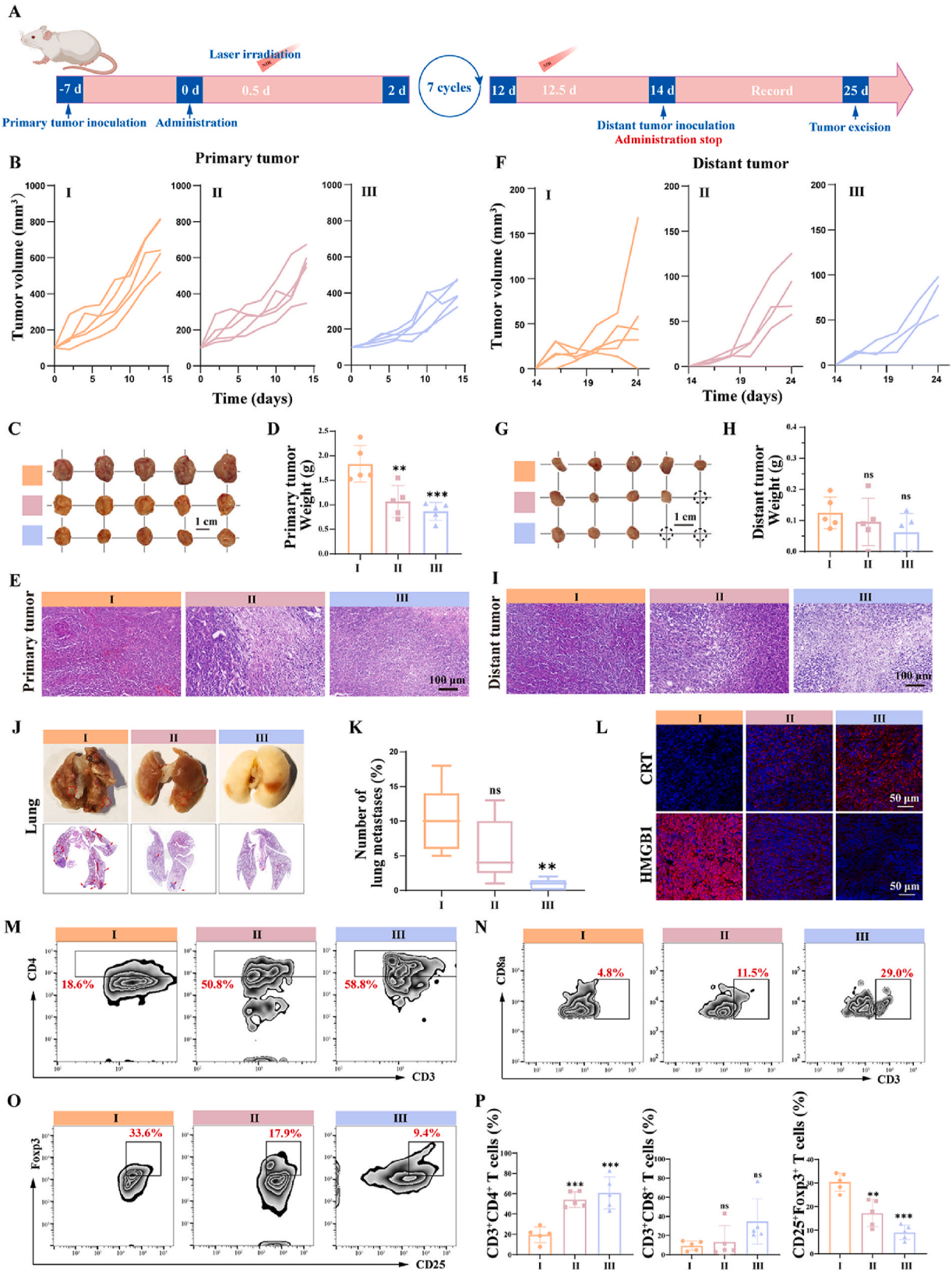

Fig. 7. Anti-tumor effect immune response of HM@Ce6@HPB@CS-5 NPs on breast cancer model. (A) Schematic diagram of the mouse treatment. (B) The 4T1 tumor growth curves with various treatments. (C) The digital images of tumors *in situ* ($n = 5$). (D) Primary tumor weight on the 25th day of administration. (E) H&E staining of *in situ* tumors. (F) Distant tumor development curves of mice after treatment period. (G) The digital images of distant tumor. (H) Distant tumor weight on the 25th day of administration. (I) H&E staining of distant tumors. (J) The digital images and H&E staining of typical lung after various treatments. (K) The number of lung metastatic nodule. (L) CRT and HMGB1 immunofluorescence of tumor ($n = 3$). (M) FCM analysis of $CD4^+$ T cells in primary tumors. (N) FCM analysis of $CD8^+$ T cells in primary tumors. (O) FCM analysis of the percentages of Tregs in primary tumors. (P) Representative quantitative analysis of $CD4^+$ T cells, $CD8^+$ T cells and Tregs ($n = 5$). I: PBS, II: CS-5, III: HM@Ce6@HPB@CS-5+L. Data are expressed as mean ± SD. $^{**}P < 0.01$. $^{***}P < 0.001$. *ns*, not significant.

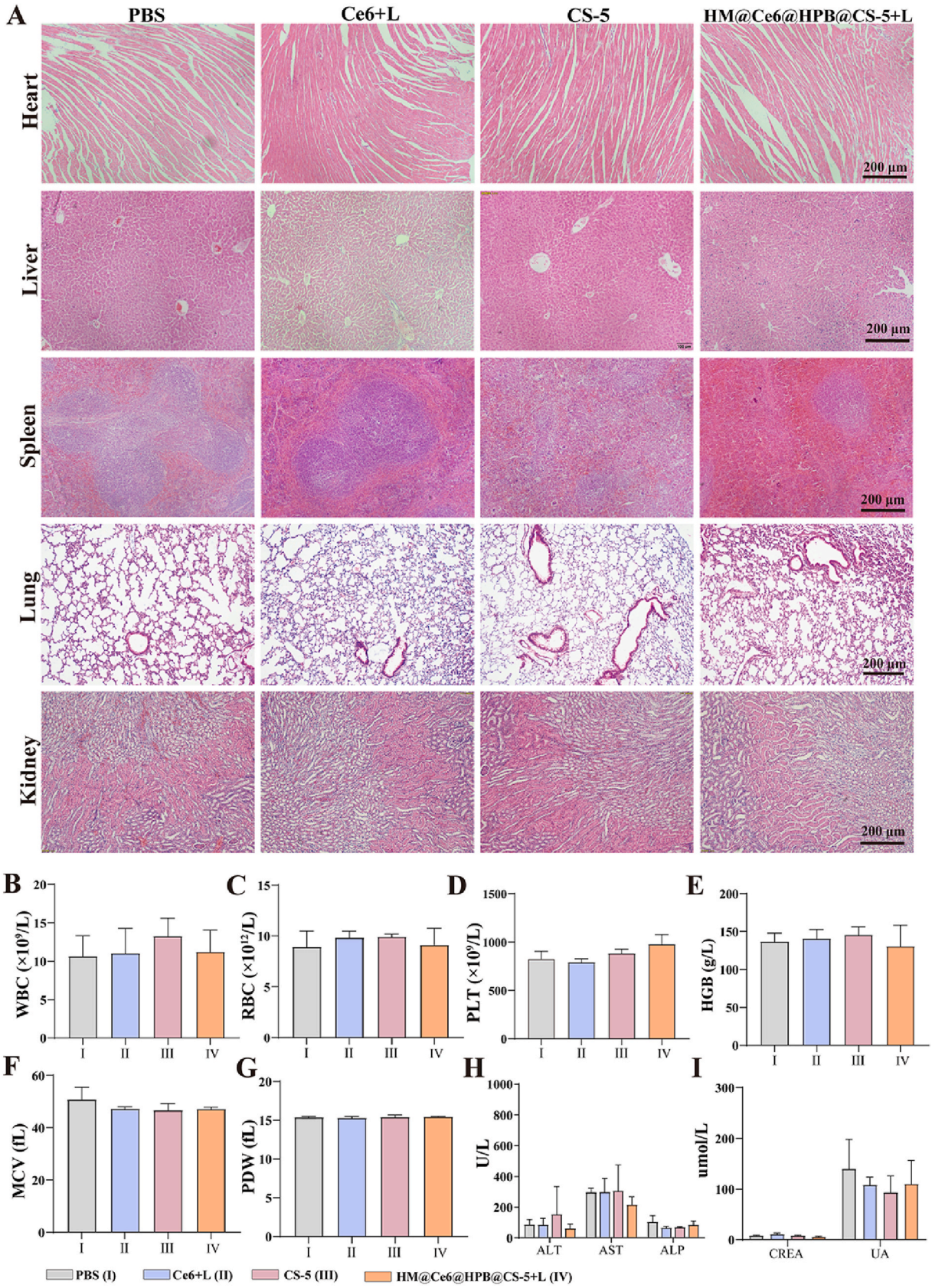

Fig. 8. *In vivo* toxicity evaluation. (A) H&E stain of the major organs after various treatments on BGC-823-bearing mice. (B–G) The blood indexes of mice after treatment with PBS, Ce6+L, free CS-5 and HM@Ce6@HPB@CS-5+L. (H and I) The levels of hepatic and kidney function markers and of mice. I: PBS, II: Ce6+L, III: CS-5, IV: HM@Ce6@HPB@CS-5+L. Data are expressed as mean ± SD ($n = 3$).

interests or personal relationships that could have appeared to influence the work reported in this paper.

Acknowledgements

This work was partially supported by the Natural Science Foundation of Hunan Province (2023JJ40130, 2024JJ8212); National Natural Science Foundation of China (82003931); Key Research and Development Projects in Ningxia Autonomous Region (2022BFH02013); The Science Project of the Education Department of Hunan Province (24B0889); Ruixin project of Hunan Provincial Maternal and Child Health Care Hospital (2023RX16).

Appendix A. Supplementary data

Supplementary data to this article can be found online at https://doi.org/10.1016/j.mtbio.2025.101684.

Data availability

Data will be made available on request.

References

[1] J. Ferlay, M. Colombet, I. Soerjomataram, D.M. Parkin, M. Piñeros, A. Znaor, et al., Cancer statistics for the year 2020: an overview, Int. J. Cancer 149 (2021) 778–789.
[2] X. Qu, D. Zhou, J. Lu, D. Qin, J. Zhou, H.-J. Liu, Cancer nanomedicine in preoperative therapeutics: nanotechnology-enabled neoadjuvant chemotherapy, radiotherapy, immunotherapy, and phototherapy, Bioact. Mater. 24 (2023) 136–152.
[3] J. Kang, J.H. Lee, H. Cha, J. An, J. Kwon, S. Lee, et al., Systematic dissection of tumor-normal single-cell ecosystems across a thousand tumors of 30 cancer types, Nat. Commun. 15 (1) (2024) 4067.
[4] K.O. Alfarouk, C.-M. Stock, S. Taylor, M. Walsh, A.K. Muddathir, D. Verduzco, et al., Resistance to cancer chemotherapy: failure in drug response from ADME to P-gp, Cancer Cell Int. 15 (1) (2015) 71.
[5] Y. Long, Z. Wang, J. Fan, L. Yuan, C. Tong, Y. Zhao, et al., A hybrid membrane coating nanodrug system against gastric cancer via the VEGFR2/STAT3 signaling pathway, J. Mater. Chem. B 9 (18) (2021) 3838–3855.
[6] J. Jia, J. Li, Q. Zheng, D. Li, A research update on the antitumor effects of active components of Chinese medicine ChanSu, Front. Oncol. 12 (2022) 1014637.
[7] Y. Liu, Y. Liang, J. Yuhong, P. Xin, J.L. Han, Y. Du, et al., Advances in nanotechnology for enhancing the solubility and bioavailability of poorly soluble drugs, Drug Des. Dev. Ther. 18 (2024) 1469–1495.
[8] P. Agostinis, K. Berg, K.A. Cengel, T.H. Foster, A.W. Girotti, S.O. Gollnick, et al., Photodynamic therapy of cancer: an update, CA Cancer J. Clin. 61 (4) (2011) 250–281.
[9] T. Jia, J. Xu, S. Dong, F. He, C. Zhong, G. Yang, et al., Mesoporous cerium oxide-coated upconversion nanoparticles for tumor-responsive chemo-photodynamic therapy and bioimaging, Chem. Sci. 10 (37) (2019) 8618–8633.
[10] X.-S. Wang, J.-Y. Zeng, M.-K. Zhang, X. Zeng, X.-Z. Zhang, A versatile Pt-based core–shell nanoplatform as a nanofactory for enhanced tumor therapy 28 (36) (2018) 1801783.
[11] P. Wang, S. Sun, G. Bai, R. Zhang, F. Liang, Y. Zhang, Nanosized Prussian blue and its analogs for bioimaging and cancer theranostics, Acta Biomater. 176 (2024) 77–98.
[12] J. Fan, Y. Qin, C. Xiao, L. Yuan, Y. Long, Y. Zhao, et al., Biomimetic PLGA-based nanocomplexes for improved tumor penetration to enhance chemo-photodynamic therapy against metastasis of TNBC, Materials Today Advances 16 (2022) 100289.
[13] Q. Xie, Y. Liu, Y. Long, Z. Wang, S. Jiang, R. Ahmed, et al., Hybrid-cell membrane-coated nanocomplex-loaded chikusetsusaponin IVa methyl ester for a combinational therapy against breast cancer assisted by Ce6, Biomater. Sci. 9 (8) (2021) 2991–3004.
[14] S. Chen, J. Fan, F. Xiao, Y. Qin, Y. Long, L. Yuan, et al., Erythrocyte membrane-camouflaged Prussian blue nanocomplexes for combinational therapy of triple-negative breast cancer, J. Mater. Chem. B 11 (10) (2023) 2219–2233.
[15] C. Xiao, C. Tong, J. Fan, Z. Wang, Q. Xie, Y. Long, et al., Biomimetic nanoparticles loading with gamabutolin-indomethacin for chemo/photothermal therapy of cervical cancer and anti-inflammation, J. Contr. Release 339 (2021) 259–273.
[16] J. Liang, C. Wang, J. Fan, Q. Xie, Z. Yu, B. Liu, et al., Hybrid membrane-camouflaged hollow prussian blue nanoparticles for shikonin loading and combined chemo/photothermal therapy of metastatic TNBC, Materials Today Advances 14 (2022) 100245.
[17] B.A. Thomas-Moore, S. Dedola, D.A. Russell, R.A. Field, M.J. Marín, Targeted photodynamic therapy for breast cancer: the potential of glyconanoparticles, Nanoscale Adv. 5 (23) (2023) 6501–6513.
[18] C. Yang, X. Liao, K. Zhou, Y. Yao, X. He, W. Zhong, et al., Multifunctional nanoparticles and collagenase dual loaded thermosensitive hydrogel system for enhanced tumor-penetration, reversed immune suppression and photodynamic-immunotherapy, Bioact. Mater. 48 (2025) 1–17.
[19] Z. Zeng, Z. Wang, S. Chen, C. Xiao, M. Liu, J. Zhang, et al., Bio-nanocomplexes with autonomous O(2) generation efficiently inhibit triple negative breast cancer through enhanced chemo-PDT, J. Nanobiotechnol. 20 (1) (2022) 500.
[20] L.F. Ye, K.R. Chaudhary, F. Zandkarimi, A.D. Harken, C.J. Kinslow, P. S. Upadhyayula, et al., Radiation-induced lipid peroxidation triggers ferroptosis and synergizes with ferroptosis inducers, ACS Chem. Biol. 15 (2) (2020) 469–484.
[21] D.M. Zhang, J.S. Liu, M.K. Tang, A. Yiu, H.H. Cao, L. Jiang, et al., Bufotalin from Venenum Bufonis inhibits growth of multidrug resistant HepG2 cells through G2/M cell cycle arrest and apoptosis, Eur. J. Pharmacol. 692 (1–3) (2012) 19–28.
[22] W. Zhang, B. Jiang, Y. Liu, L. Xu, M. Wan, Bufotalin induces ferroptosis in non-small cell lung cancer cells by facilitating the ubiquitination and degradation of GPX4, Free Radic. Biol. Med. 180 (2022) 75–84.
[23] X. Zhang, S. Sui, L. Wang, H. Li, L. Zhang, S. Xu, et al., Inhibition of tumor propellant glutathione peroxidase 4 induces ferroptosis in cancer cells and enhances anticancer effect of cisplatin, J. Cell. Physiol. 235 (4) (2020) 3425–3437.
[24] C. Xiao, Y. Sun, J. Fan, W. Nguyen, S. Chen, Y. Long, et al., Engineering cannabidiol synergistic carbon monoxide nanocomplexes to enhance cancer therapy via excessive autophagy, Acta Pharm. Sin. B 13 (11) (2023) 4591–4606.
[25] J. Lin, J.-H. Lin, T.-Y. Yeh, J.-H. Zheng, E.-C. Cho, K.-C. Lee, Fabrication of hyaluronic acid with graphene quantum dot as a dual drug delivery system for cancer therapy, FlatChem 44 (2024) 100607.
[26] H. Zhou, P. You, H. Liu, J. Fan, C. Tong, A. Yang, et al., Artemisinin and Procyanidins loaded multifunctional nanocomplexes alleviate atherosclerosis via simultaneously modulating lipid influx and cholesterol efflux, J. Contr. Release : Off. J. Control. Release. Soc. 341 (2022) 828–843.
[27] B. Dutta, K.C. Barick, P.A. Hassan, Recent advances in active targeting of nanomaterials for anticancer drug delivery, Adv. Colloid Interface Sci. 296 (2021) 102509.
[28] Z. Zeng, Z. Wang, S. Chen, C. Xiao, M. Liu, J. Zhang, et al., Bio-nanocomplexes with autonomous O(2) generation efficiently inhibit triple negative breast cancer through enhanced chemo-PDT, J. Nanobiotechnol. 20 (1) (2022) 500.
[29] L.-J. Peng, H.-Y. Zhou, C.-Y. Zhang, F.-Q. Yang, Study on the peroxidase-like activity of cobalt phosphate and its application in colorimetric detection of hydrogen peroxide, Colloids Surf. A Physicochem. Eng. Asp. 647 (2022) 129031.
[30] C.-P. Liu, T.-H. Wu, C.-Y. Liu, K.-C. Chen, Y.-X. Chen, G.-S. Chen, et al., Self-supplying O2 through the catalase-like activity of gold nanoclusters for photodynamic therapy against hypoxic, Cancer Cells (Cold Spring Harbor) 13 (26) (2017) 1700278 [J].
[31] J. Mu, L. Zhang, M. Zhao, Y. Wang, Catalase mimic property of Co3O4 nanomaterials with different morphology and its application as a calcium sensor, ACS Appl. Mater. Interfaces 6 (10) (2014) 7090–7098.
[32] R.H. Fang, A.V. Kroll, W. Gao, L. Zhang, Cell Membr. Coating. Nanotechnol. J 30 (23) (2018) 1706759.
[33] X. Han, C. Gong, Q. Yang, K. Zheng, Z. Wang, W. Zhang, Biomimetic nano-drug delivery system: an emerging platform for promoting tumor treatment, Int. J. Nanomed. 19 (2024) 571–608.
[34] T. Hou, Z. Li, Y. Zhao, W.-G. Zhu, Mechanisms controlling the anti-neoplastic functions of FoxO proteins, Semin. Cancer Biol. 50 (2018) 101–114.
[35] S. Qiao, Y. Kang, X. Tan, X. Zhou, C. Zhang, S. Lai, et al., Nanomaterials-induced programmed cell death: focus on mitochondria, Toxicology 504 (2024) 153803.
[36] Y. Li, J. Liu, Y. Chen, R.R. Weichselbaum, W. Lin, Nanoparticles synergize ferroptosis and cuproptosis to potentiate cancer immunotherapy, Adv. Sci. (2024) e2310309.
[37] N. Liu, Q. Lin, Z. Huang, C. Liu, J. Qin, Y. Yu, et al., Mitochondria-targeted prodrug nanoassemblies for efficient ferroptosis-based therapy via devastating ferroptosis defense systems, ACS Nano 18 (11) (2024) 7945–7958.
[38] F. Ursini, M. Maiorino, Lipid peroxidation and ferroptosis: the role of GSH and GPx4, Free Radic. Biol. Med. 152 (2020) 175–185.
[39] S. Zeng, C. Chen, L. Zhang, X. Liu, M. Qian, H. Cui, et al., Activation of pyroptosis by specific organelle-targeting photodynamic therapy to amplify immunogenic cell death for anti-tumor immunotherapy, Bioact. Mater. 25 (2023) 580–593.
[40] A.A. Bhat, R. Thapa, O. Afzal, N. Agrawal, W.H. Almalki, I. Kazmi, et al., The pyroptotic role of Caspase-3/GSDME signalling pathway among various cancer: a Review, Int. J. Biol. Macromol. 242 (Pt 2) (2023) 124832.
[41] D. Li, S. Liu, Y. Ma, S. Liu, Y. Liu, J. Ding, Biomaterials that induce immunogenic cell death 7 (5) (2023) 2300204.
[42] I. Ferreira-Faria, S. Yousefiasl, A. Macário-Soares, M. Pereira-Silva, D. Peixoto, H. Zafar, et al., Stem cell membrane-coated abiotic nanomaterials for biomedical applications, J. Contr. Release 351 (2022) 174–197.
[43] Y. Zi, K. Yang, J. He, Z. Wu, J. Liu, W. Zhang, Strategies to enhance drug delivery to solid tumors by harnessing the EPR effects and alternative targeting mechanisms, Adv. Drug Deliv. Rev. 188 (2022) 114449.
[44] B. Medeiros, A.L. Allan, Molecular mechanisms of breast cancer metastasis to the lung: clinical and experimental perspectives, Int. J. Mol. Sci. 20 (9) (2019).